White Rose Research Online

eprints@whiterose.ac.uk
https://eprints.whiterose.ac.uk
Universities of Leeds, Sheffield and York

Deposited via The University of Sheffield.

White Rose Research Online URL for this paper:
https://eprints.whiterose.ac.uk/id/eprint/247882/

Version: Published Version

Article:
Cuervo, P.A., Toro, A., Meza, J.M. et al. (2026) Apparent contact width modification through deterministic surface texturing: friction and wear response in rolling sliding line contacts. Eng, 7 (11). 595. ISSN: 2673-4117

https://doi.org/10.3390/eng7110595

Reuse
This article is distributed under the terms of the Creative Commons Attribution (CC BY) licence. This licence allows you to distribute, remix, tweak, and build upon the work, even commercially, as long as you credit the authors for the original work. More information and the full terms of the licence here: https://creativecommons.org/licenses/

Takedown
If you consider content in White Rose Research Online to be in breach of UK law, please notify us by emailing eprints@whiterose.ac.uk including the URL of the record and the reason for the withdrawal request.

UNIVERSITY OF LEEDS
University of Sheffield
UNIVERSITY of York

eng

MDPI

Article

Apparent Contact Width Modification Through Deterministic Surface Texturing: Friction and Wear Response in Rolling Sliding Line Contacts

Paula A. Cuervo [1,*], Alejandro Toro [2], Juan M. Meza [2,3], Roger Lewis [4] and Luis H. Martínez [1]

[1] Grupo de Investigación en Diseño y Manufactura—DIMA, Universidad Industrial de Santander, Bucaramanga 680002, Colombia; lhmarpal@uis.edu.co
[2] Tribology and Surfaces Group, Universidad Nacional de Colombia, Medellín 050034, Colombia; aotoro@unal.edu.co (A.T.); jmmezam@unal.edu.co (J.M.M.)
[3] Design of Advanced Composites Group-DADCOMP, Universidad Nacional de Colombia, Medellín 050034, Colombia
[4] School of Mechanical, Aerospace and Civil Engineering, University of Sheffield, Sheffield S1 3JD, UK; roger.lewis@sheffield.ac.uk
* Correspondence: pacuevel@uis.edu.co

Abstract

To understand the tribological behaviour of rolling–sliding pairs with textured surfaces, two cylinders in contact were modified to account for the introduction of deterministic patterns. The experimental work developed was applied to study the effect of surface texture on the tribological response of Hertzian line contact tested in a twin-disc machine. Contact conditions used were based around a wheel/rail interface. It was found that the contact semi-width increased in the textured discs, which led to a reduction in the apparent contact pressure and subsequent effects on the stick/slip ratio for each percentage of applied slip. The increases in contact widths and the corresponding reduction in contact pressures were verified through finite element numerical simulations, assuming linear elastic material behaviour and a surface-to-surface contact formulation. The study shows that it is possible to reach a constant friction condition at lower slip percentages in textured surfaces. This could be a benefit in addressing problems associated with friction management, that is, to design the texture for contacts where it is difficult to control friction and also to be able to reduce contact pressures. Quantitatively, the apparent contact width increased by approximately 18% for the diamond-textured configuration, while the calculated load-bearing surface contact area remained nearly constant. At 1% slip, the mean crack length decreased by approximately 18% for both textured configurations, whereas the depth of the heavily deformed layer decreased by approximately 46% and 91% for the diamond and slot textures, respectively, compared with the non-textured surface.

Keywords: coefficient of friction; contact mechanics; disc-on-disc testing; deterministic surfaces; $T\gamma$ approach

Academic Editors: Kai Wang, Jingmang Xu and Yao Qian

Received: 23 September 2026
Revised: 16 October 2026
Accepted: 29 October 2026
Published: 1 November 2026

Copyright: © 2026 by the authors. Licensee MDPI, Basel, Switzerland. This article is an open access article distributed under the terms and conditions of the Creative Commons Attribution (CC BY) license.

1. Introduction

The evaluation of contact stresses, contact area dimensions, and tangential contact behaviour under rolling–sliding conditions has been widely studied using Hertzian, non-Hertzian, and semi-Hertzian models for contacting cylinders [1,2]. Hertzian equations,

developed in the nineteenth century, are commonly used to model contact mechanics but are primarily applicable to frictionless, normally loaded contacts between smooth elastic solids [3]. Regarding contact models involving traction forces and wear, important contributions have been made by Kalker, who developed several theories to solve normal and tangential contact problems, including Linear Theory, Strip Theory, Empirical Theory, Simplified Theory, and Exact Three-Dimensional Rolling Contact Theory [2,4–7]. Nevertheless, these classical formulations do not explicitly account for the effect of a deterministic surface pattern within the contact patch on the tribological response of the system. In this context, several theoretical and numerical investigations have focused on understanding the influence of statistical roughness parameters on contact conditions [5,8–16]. However, despite these advances, the quantitative relationship between deterministic surface texture geometry, apparent contact width, stress redistribution, and tribological behaviour under dry rolling–sliding line contact conditions remains insufficiently characterized.

In many tribological interfaces, there is a need to predict and control friction and wear over time, and one approach to achieving this objective involves introducing deterministic surface texture patterns. This has generated several research lines focused on improving frictional performance and controlling wear and energy consumption [17,18]. Bio-inspired designs have also been developed [19–30], and different techniques have been proposed to manufacture textured surfaces on a wide range of materials [31–41].

Numerous industrial applications of deterministic surfaces have been investigated to improve tribological performance [17,18,31,32,34,42–47]. Particular examples include textured piston ring assemblies in internal combustion engines [48] and surface dimples on cylinder liners [49]. More recently, Vencl et al. [50] and Lu and Wood [51] reviewed the influence of surface texturing on friction and wear, highlighting the importance of texture geometry, operating conditions, and lubrication mechanisms. Rosenkranz et al. [52] also discussed the applicability and limitations of surface texturing in rolling and sliding contacts. Although these studies demonstrate the potential of deterministic textures, their tribological response depends on the specific mechanical and interfacial mechanisms involved.

Previous investigations have also examined the relationship between surface texture geometry and contact mechanics. Prodanov et al. [53] investigated the mechanical behaviour of laser-textured surfaces, while Gachot et al. [54] analyzed the influence of surface pattern alignment and geometry on dry friction. More recently, Jiang et al. [55] studied a friction-reduction mechanism associated with the sublinear dependence of friction on normal load in textured PTFE–steel contacts, where the reduction in nominal load-bearing area increases local contact pressures. In contrast to the specific friction-reduction mechanism investigated by Jiang et al. [55], the present study focuses on modifications of apparent Hertzian contact width and their relationship with stress distribution, friction, and wear under dry rolling–sliding conditions between railway steels. This distinction highlights the importance of contact configuration and texture geometry in determining the mechanical and tribological response.

Therefore, the physical mechanisms and contact configurations considered in these investigations are different, demonstrating the importance of analyzing surface texture effects according to the specific contact conditions.

The present research represents a continuation and further development of the investigation presented by Cuervo et al. at the 12th International Conference on Contact Mechanics and Wear of Rail/Wheel Systems (CM2022) [56]. In the present work, tribological tests were carried out using a twin-disc machine with deterministically textured surfaces under rolling–sliding conditions. In addition, analytical and numerical investigations were performed using MATLAB (version R20XX; MathWorks, Natick, MA, USA) and PrePoMax v2.3 with the CalculiX 2.2 solver. The modified Hertzian formulation

considers the shape and distribution of texture elements, allowing the calculation of apparent contact dimensions and contact stresses. Finite element simulations were used to verify the modifications in contact geometry and stress distributions under normal elastic loading, without simulating friction or wear evolution.

Furthermore, a geometrical–analytical correlation between apparent contact semi-width and stable coefficient of friction (COF) was established using experimental results from 15 deterministic texture configurations, including the six initial geometries considered in the experimental design. The experimental investigation was also used to evaluate the influence of deterministic surface textures on traction, friction, wear, and rolling contact fatigue. A set of equations based on the $T\gamma$ approach, commonly used in wheel–rail interface studies to relate contact energy and wear, was employed to evaluate wear behaviour for selected diamond and slot texture configurations. The contact conditions were selected to represent relevant mechanical and tribological characteristics of the wheel–rail interface using R400HT rail and E8 wheel materials.

The main contribution of this study is the quantitative investigation of the relationship between deterministic texture geometry, apparent contact width, contact stress distribution, and friction and wear behaviour under dry rolling–sliding conditions. By combining a modified Hertzian contact formulation, finite element verification of contact geometry and stress distributions, experimental contact-width measurements, a geometrical–analytical correlation between apparent contact semi-width and stable COF, and twin-disc tribological testing, the study provides a quantitative mechanical interpretation of the influence of deterministic surface texture geometry on contact conditions and tribological behaviour.

The scientific significance of this investigation lies in providing a contact mechanics interpretation of the influence of deterministic surface texturing on dry rolling–sliding behaviour. Unlike studies primarily focused on friction and wear responses under pure sliding or lubricated conditions, the present work examines how deterministic texture geometry modifies the apparent contact dimensions while maintaining an approximately constant total load-bearing surface contact area. By combining a modified Hertzian contact formulation, static finite element simulations, and experimental twin-disc testing, the study establishes a relationship between contact geometry, stress redistribution, traction behaviour, and wear-related subsurface damage. These findings provide a mechanical basis for understanding how deterministic textures can contribute to friction and wear management without necessarily requiring a reduction in the coefficient of friction. The results are relevant to the development of geometry-based dry friction modification technologies for railway wheel–rail contacts and other rolling–sliding tribological systems.

2. Experimental Work

The tribological tests were performed using a twin-disc testing machine under dry conditions with 4905 N normal load and nominal 400 rpm rotational speed. Under these conditions the maximum contact stress at the surface is 1.3 GPa and the contact semi-width 0.2735 mm for non-textured samples, so it is representative of the typical wheel–rail contact conditions in many railway systems. A detailed description of the testing machine can be found elsewhere [57].

The tangential force between the discs was measured during the tests with a torque transducer installed on the wheel disc axis to calculate the coefficient of traction (COT) and the energy dissipated in the contact per unit volume ($T\gamma$ approach). Ten different slip ratios varying from 0 to 20% were used. Four tests were performed for each slip value.

The wheel disc was driven faster than the rail disc to replicate traction conditions between the wheels and the rails in the field. The tangential contact force is obtained from

the surface radius and the torque measurement. The COT was calculated with the tangential force and the normal force applied.

To determine the coefficient of friction (COF), i.e., the maximum, stable COT that is obtained after a given percentage of slip where the contact is saturated with slip [58–65], COT versus slip curves were obtained for the different tribological pairs. The mass loss of the discs after the tests were measured and the wear rate per cycle was calculated. Wear rate versus $T\gamma/A$ curves were also obtained, where T corresponds to the tangential force at the contact, γ is the slip and A is the size of the contact patch [57,59,60].

Both rail and wheel discs had a rolling surface outer diameter of 47 mm and the width of the contact zone was 9 mm. Only rail samples were textured. The test specimens were extracted from wheels (E8, standard grade) and rails (hardened premium R400HT grade), see EN 13262 standard [66] for the wheel material. Tensile tests for both materials were performed in accordance with ASTM E8. The chemical composition of the materials, measured by optical emission spectroscopy (OES), can be found in previous reports [67,68]. The mechanical properties are shown in Table 1.

Table 1. Mechanical properties of rail and wheel materials [67,68].

Material	Modulus of Elasticity E (GPa)	Poisson's Ratio ν	Hardness, HV
Rail R400HT	212	0.30	400 ± 10
Wheel E8	199	0.28	260 ± 7

Note: Tensile testing of both materials was performed in accordance with ASTM E8.

The surface finishing for the wheel samples was achieved by lathe turning with a tungsten carbide pad tool. The corresponding roughness parameters obtained are shown in Table 2. Roughness measurements were carried out using a Mitutoyo SV 4000 roughness station. A cut-off of 0.8 mm, a total sampling length of 8.0 mm and a sampling rate of 0.5 m/s were used. In all cases, five measurements were made. The surface quality parameters were measured according to the ISO 4287 standard with a Gaussian filter [69]. The analyzed parameters were Ra (arithmetic mean deviation of the profile), Rq (root mean square deviation of the assessed profile), Rp (maximum profile peak height), Rv (maximum profile valley depth), Rsk (Skewness of the assessed profile), and Rku (kurtosis of the assessed profile: sharpness of the height distribution, defined on the sampling length).

Table 2. Roughness parameters of wheel samples after lathe turning.

Ra (μm)	Rq (μm)	Rp (μm)	Rv (μm)	Rsk	Rku
0.5	0.8	0.867	0.951	−0.197	2.249

Surface roughness measurements were performed to verify the quality and consistency of the initial machined surface finish before the fabrication of the deterministic textures. All specimens were prepared under comparable finishing conditions, with a nominal Ra value of approximately 0.5 μm. Five roughness measurements were performed per disc, using four discs per experimental condition, resulting in a total of 20 roughness measurements per experimental condition. The purpose of this characterization was to establish comparable initial surface conditions and minimize the influence of machining-related roughness differences, allowing the effects of deterministic texture geometry on contact mechanics and tribological behaviour to be investigated.

2.1. Texture Designs

Two texture designs were implemented, as shown in Figure 1. These were selected based on the results from previous work [21,29,70], in which the use of deterministic surfaces led to reductions in energy consumption and wear under tribological testing.

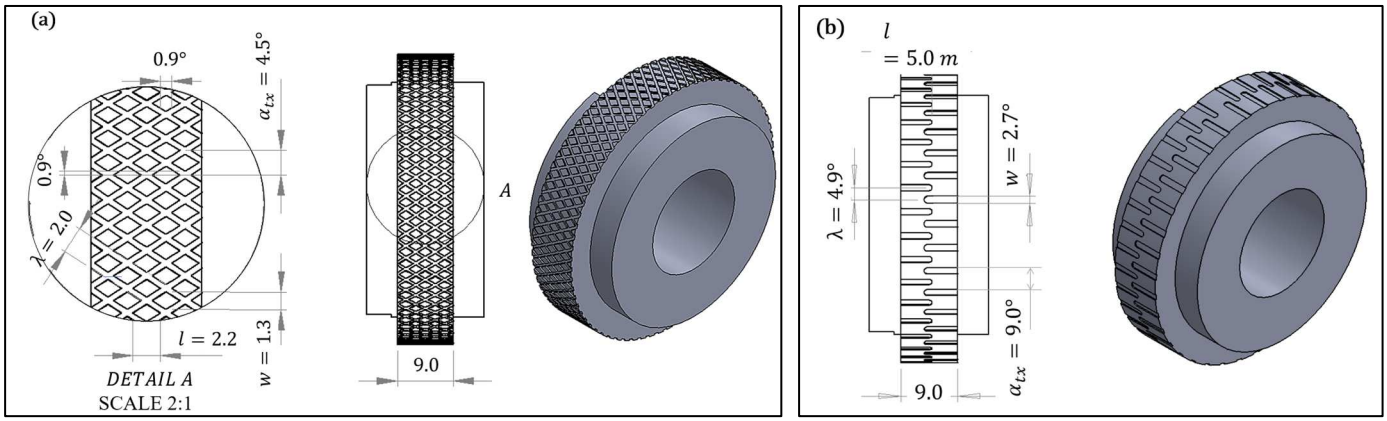


Figure 1. Texture design for rail discs: (**a**) Diamond texture- high scale; (**b**) Slot texture- low scale. Linear dimensions in mm, except as indicated in the dimensions.

The first texture consisted of arrays of diamond-like elements, while the second one was a distribution of slots orthogonal to the rolling–sliding direction of the samples. The scale of the texture elements was of the order of millimetres. Only the rail discs were selected for surface texturing as they have greater hardness and elastic modulus than the wheel. This was in order to have a contact with deformation in the elastic region [13,71–75].

Table 3 shows the values of the relevant texture parameters for both texture designs and the three different "scales" used. The selected parameters were w and l, which are the length and width of the texture elements, respectively, and the separation of the texture elements, or pitch, is λ [21,29,70]. The "diamond" texture was obtained by knurling with a knurl selected according to the DIN 82 standard. The M7 INTEGI model for radial machining was implemented with 10 mm width [76–78], which gave a separation between the diamond diagonals of l = 2.2 mm, w = 1.3 mm, and λ = 2.0 mm (see Figure 2a). After knurling, the surface was ground to remove burrs and obtain a surface roughness of Ra = 0.5 μm, equal to the surface roughness of the wheel's contact surface, and then polished with ASTM n. 2000 sandpaper. The knurling process was carried out with a cutting speed between 20 and 25 m/min, radial feed between 0.04 and 0.08 mm/rev and longitudinal feed 0.1 mm/rev.

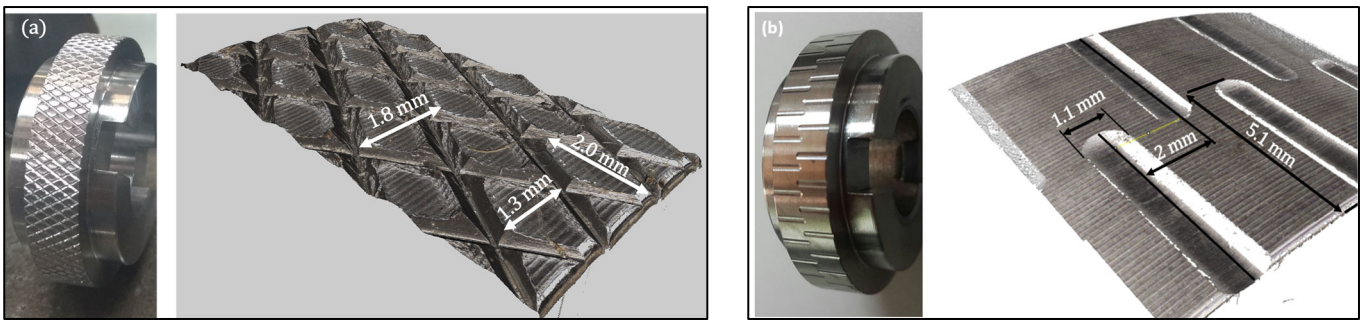


Figure 2. Aspect of textured and linear dimensions rail discs: (**a**) Diamond texture (high scale); (**b**) Slot texture (low scale).

Table 3. Pattern measurements at different scales.

Pattern	Diamond Texture (Tx_D)			Slot Texture (Tx_S)		
	Tx_D High Scale	Tx_D Medium Scale	Tx_D Low Scale	Tx_S High Scale	Tx_S Medium Scale	Tx_S Low Scale
w (mm)	1.3	1.2	0.7	6.2	3.1	1.1
l (mm)	2.2	1.6	1.0	5.0	5.0	5.0
λ (mm)	2.0	1.5	0.8	11.4	5.6	2.0
l/w	1.7	1.3	1.4	0.8	1.6	4.5

The slot texture was obtained using a computerized numerical control (CNC) machine with a round milling cutter (radius 3 mm) operating at 10,000 RPM, with a feed of 0.26 mm/min and depth of cut between 0.05 mm and 0.08 mm. The software CAM SprutCAM 11 ® was used to plan the machining strategy (see Figure 2b) [30].

2.2. Characterization of the Textured Surfaces

The typical aspect of the textured rail discs can be seen in Figure 2 where the angular dimensions of the diamond pattern were converted into equivalent linear dimensions for clarity and are reported in millimetres. A relative variation of less than 5% for knurling and 6% for CNC machining was found between the designed and measured dimensions of the samples. For the discs textured by knurling the contact surface of the samples had a hardness of 404 HV ± 10 HV (see Figure 3a). However, in the deformed areas (the "valleys" in Figure 3b), a higher value of 580 HV ± 10 HV was measured up to 50 µm from the surface. In contrast, there was no change in the hardness of the CNC-machined specimens, with a measured average value of 402 ± 10 HV (see Figure 3c).

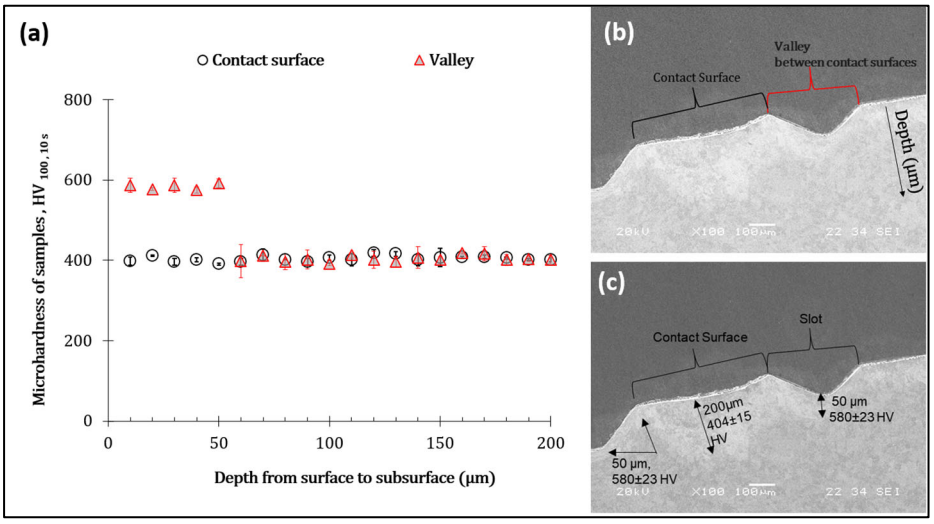


Figure 3. Characterization of the textured surfaces: (**a**) Variation in microhardness with distance to the surface; (**b**) Cross section of knurled specimen (diamond texture); (**c**) cross section of CNC-machined specimen (slot texture).

3. Contact Model Modification for Textured Surfaces

Two-dimensional Hertz equations for the contact patch and stress distribution of two cylinders in contact were modified to account for the introduction of deterministic surfaces. These equations were adjusted to include the geometry of deterministic patterns. The theoretical framework developed was applied to study the effect of surface texture on the tribological response of a wheel–rail pair tested in a twin-disc machine. Further details are presented in the results and the Appendix A.

3.1. Contact Geometry Configuration

The texture patterns were parameterized according to a reference system fixed at the surface of the samples (see Figure 4) and the analysis was carried out for each position in the x-axis direction which generates lines of contact. The diamond textured surface is not continuous in the y direction with a pattern repeating with an angle interval α_{tx} that starts at an angle $\alpha_{i_{tx}}$ and ends at the angle $\alpha_{f_{tx}}$, that is, $\alpha_{i_{tx}} \leq \alpha_{tx} \leq \alpha_{f_{tx}}$ (see Figure 4b,c). This texture is composed of two diamond patterns P1 and P2 as shown in Figure 4b. For other textures P_j will denote each pattern.

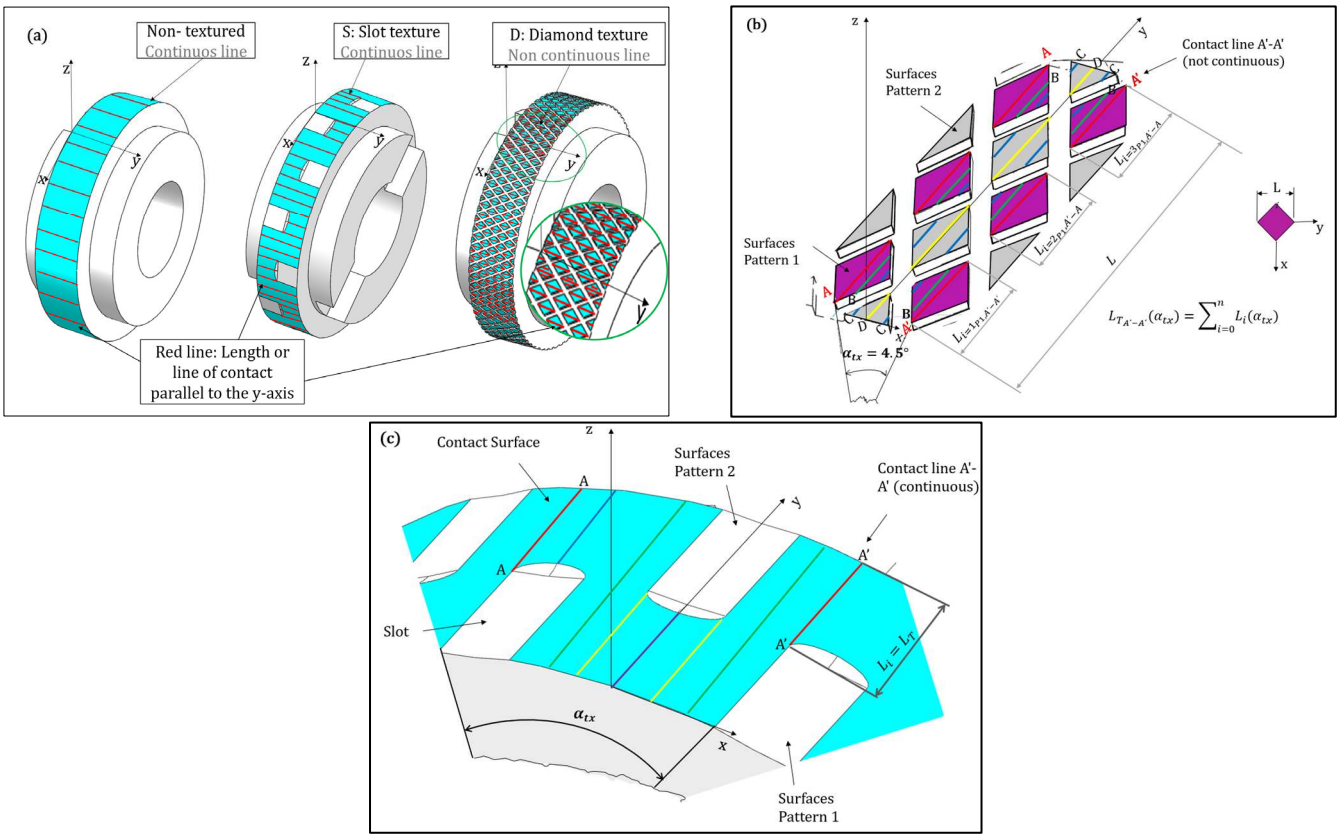


Figure 4. Illustrative contact lines: (**a**) The contact length variation continuous and non-continuous; (**b**) Pattern from 0° a 4.5° of the contact line A-A, $\alpha_{tx} = 0°$, n = 3; (**c**) Example of continuous contact length for texture with deterministic pattern slots.

As illustrated in Figure 4, if a textured cylinder (rail) is brought into contact with a non-textured one (wheel), both the actual contact length (L_T) (the sum of the contact lengths in each diamond L_i) and the contact area will be a function of the position of the contact line, i.e., of $\boldsymbol{x}$ or the angle α. In the diamond texture pattern, for instance, a texture element—or diamond—is given every 4.5° and n is the number of diamonds (spots) the contact line passes through. Figure 4b shows the variation in the contact length for three angles ($0° \leq \alpha_{tx} \leq 4.5°$). The contact line A-A ($\alpha_{i_{tx}} = 0°$) passes through three spots, hence n = 3; finally, contact line A'-A' ($\alpha_{f_{tx}} = 4.5°$) makes contact with three diamonds.

3.2. Contact Width Measurement

To validate the predictions of the modified contact model, the contact width was measured experimentally using Fuji Prescale HHS pressure-sensitive film (super high pressure) (Fujifilm Corporation, Tokyo, Japan). Direct measurement of the metal–metal contact area is not feasible due to the small size of the contact and the high contact

pressures involved; therefore, a pressure-sensitive film was employed to visualize the contact region.

The wheel surface was covered with the Fuji Prescale HHS film, which changes colour intensity as a function of the applied pressure, allowing the contact area to be identified. The thickness of the film was 100 μm. It should be noted that the film exhibits viscoelastic behaviour, which introduces additional compliance and leads to larger measured contact widths compared to an ideal elastic metal–metal contact.

Consequently, the experimental measurements are not intended to provide a direct quantitative validation of the absolute contact widths predicted by the model, but rather to validate the ability of the model to capture the relative influence of surface texturing on the contact width. The experimental set-up is shown in Figure 5.

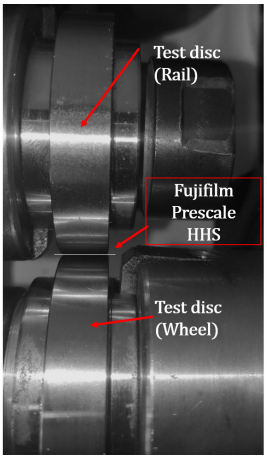


Figure 5. Set-up for contact width measurement with Fujifilm Pre-scale HHS film on the twin disc testing machine.

3.3. Finite Element–Based Validation of the Contact Model

A finite element (FE) model of the disc contact was constructed in PrePoMax v2.3 using the CalculiX 2.2 solver (see Figures 6a and 7a). Material behaviour was described by a linear elastic isotropic constitutive law, which is a reasonable assumption given that the analysis focuses on the initial elastic response prior to the onset of plastic deformation. Spatial discretization was performed using ten-node quadratic tetrahedral elements (C3D10), which provide higher accuracy in capturing stress gradients and contact interactions compared to linear elements.

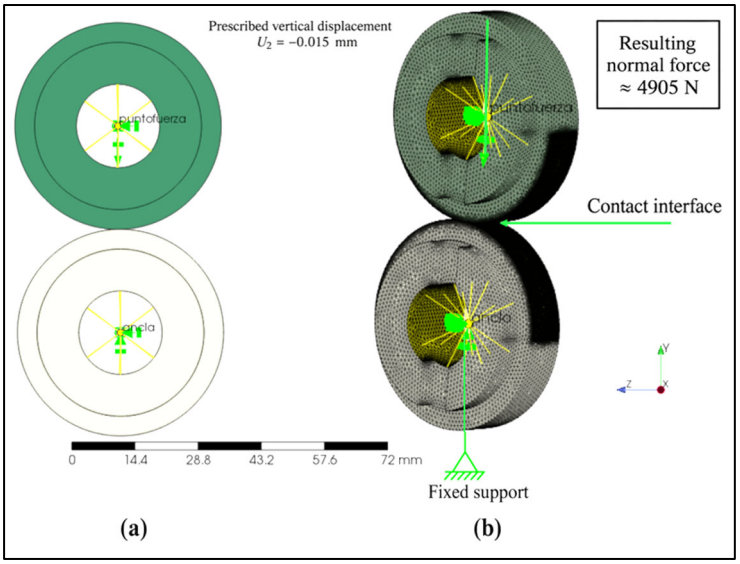


Figure 6. Finite element model of the smooth-to-smooth contact configuration: (**a**) geometrical model of the contacting discs; (**b**) finite element mesh and boundary conditions, showing the prescribed vertical displacement (U2 = −0.015 mm), the fixed support, and the contact interface. The resulting normal contact force was approximately 4905 N.

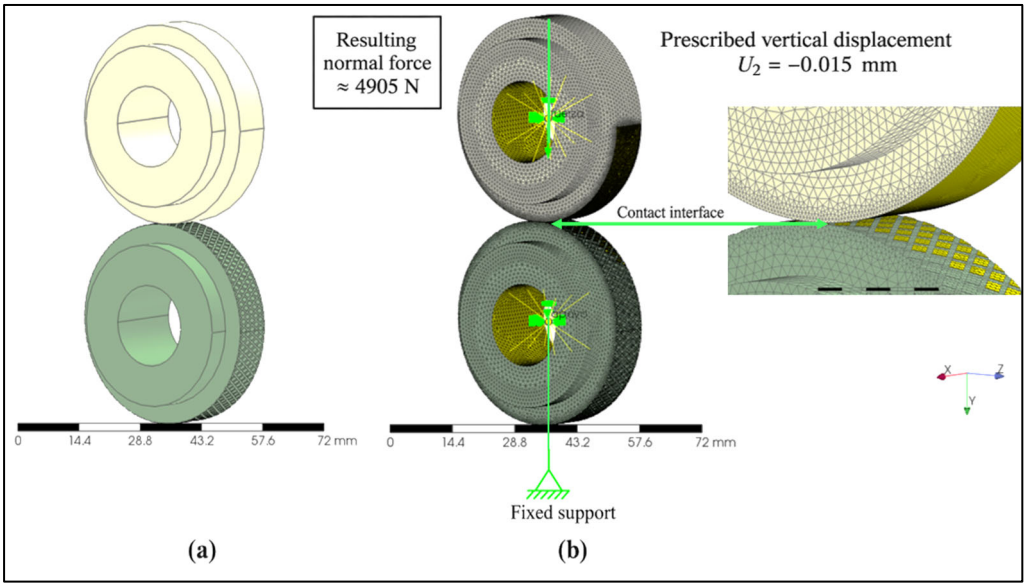


Figure 7. Finite element model of the smooth-to-diamond-textured contact configuration: (**a**) geometrical model of the contacting discs; (**b**) finite element mesh, boundary conditions, and enlarged view of the textured contact interface. The applied displacement was adjusted to obtain a resulting normal contact force of approximately 4905 N.

A mesh sensitivity study was conducted to ensure numerical convergence, revealing that approximately 400,000 elements per specimen were required to obtain mesh-independent results (see Figures 6b and 7b). Special attention was given to the contact interface, where localized mesh refinement was applied using a characteristic element size of 0.08 mm. This refinement was necessary to accurately capture the steep stress and pressure gradients inherent to contact problems.

The contact interaction was modelled using a surface-to-surface formulation with hard contact behaviour in the normal direction, thereby strictly preventing interpenetration between the contacting bodies. The Diamond texture (Tx_D), High scale specimen was defined as the slave surface to ensure accurate enforcement of contact constraints against the geometrically smoother counterpart.

The numerical analysis was limited to two configurations, namely: smooth-to-smooth contact (see Figure 6) and smooth-to-Diamond texture (Tx_D), High scale contact (see Figure 7). The imposed displacement was adjusted to reproduce the experimentally applied normal load, ensuring consistent loading conditions between the numerical and experimental configurations. For both the smooth-to-smooth and smooth-to-Diamond texture (Tx_D), High scale configurations, calibration resulted in a normal contact force of 4905 N. The boundary conditions were applied through reference points coupled to the respective disc surfaces. The lower disc was constrained through a fixed reference point, while a prescribed vertical displacement was applied to the upper disc. For the smooth-to-smooth configuration, a displacement of −0.015 mm in the global Y-direction resulted in a normal reaction force of approximately 4902.4 N, closely matching the nominal experimental load of 4905 N. The remaining translational and rotational degrees of freedom at the upper reference point were constrained. The same displacement-controlled loading

approach was adopted for the textured configuration to reproduce the target normal contact load.

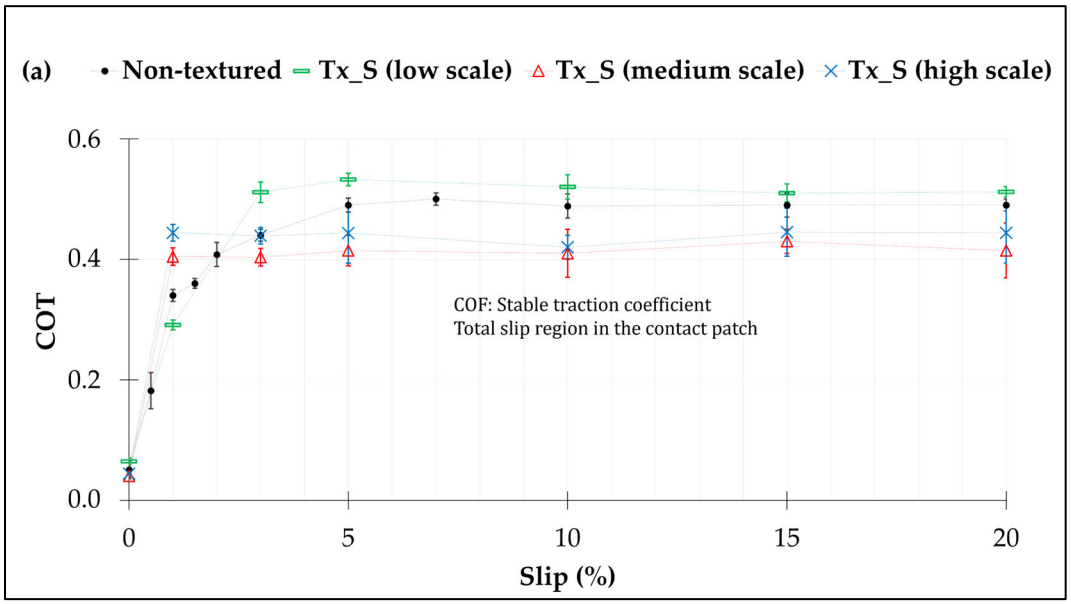
The finite element analysis was restricted to static normal loading within a linear-elastic framework. Its purpose was to evaluate the influence of deterministic surface texturing on the apparent contact width, contact area, and distribution of contact stresses and pressures. The model was not intended to simulate cyclic loading, plastic deformation, or wear. Although localized yielding may occur near texture edges, its evaluation requires an elastoplastic formulation and is beyond the scope of the present numerical analysis.

It is important to note that the texture elements studied present characteristic contact areas above 5 mm², placing them well above the micro-roughness scale at which Hertzian theory is known to break down. The validity of the modified Hertzian contact equations at this scale is confirmed by the multi-method agreement observed between the analytically predicted contact width, the FEM-computed contact width, and the contact width measured experimentally using Fuji Prescale HHS film. The agreement between the analytical predictions, finite element results, and experimental contact width measurements supports the predicted apparent contact-width trends within the adopted elastic approximation. However, this agreement does not exclude the possibility of localized yielding under the applied normal load.

3.4. Tribological and Contact Mechanical Behaviour

3.4.1. Tribological Response

The coefficient of traction (COT) versus slip percentage for all textures is shown in Figure 8, where changes in COT are evident for the different textures.



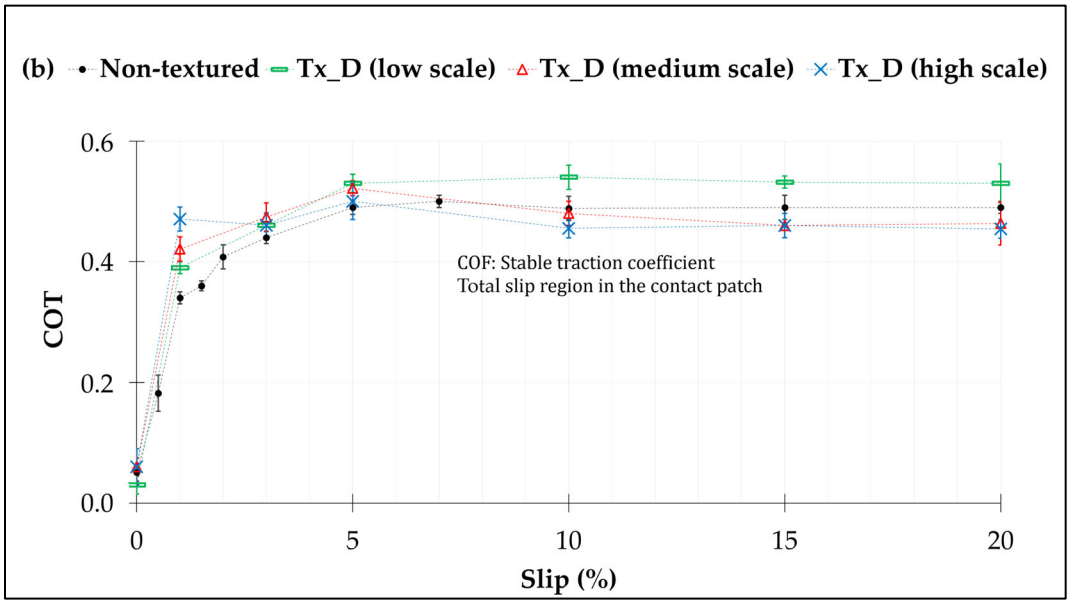


Figure 8. Variation in the coefficient of traction (COT) with slip percentage for different deterministic surface textures: (**a**) Diamond texture (Tx_D); (**b**) Slot texture (Tx_S).

The COT–slip curves were interpreted according to Carter's classical rolling–sliding contact theory, which describes the evolution of tangential traction as the relative proportions of adhesion and slip regions change within the contact. The coefficient of traction (COT) represents the ratio of tangential to normal force at each slip percentage under combined rolling–sliding conditions. The coefficient of friction (COF) corresponds to the stable limiting value identified when the COT–slip curve reaches saturation. This approach enables the traction response to be characterized throughout the investigated slip range and the slip percentage associated with friction stabilization to be determined for each surface configuration, as shown in Figure 8 and Table 4.

Table 4. Coefficients of friction (saturated traction coefficient), slip (initial force-slip gradient) and traction coefficient.

Test		Coefficient of Friction (COF), μ	Creep Coefficient (Slope Gradient)	Creep at Which Full Slip Was Achieved, (%)	Coefficient of t (COT) 1% Slip
Non-textured		0.49 ± 0.02	0.29	5	0.34 ± 0.01
Diamond texture (Tx_D)	High scale	0.46 ± 0.02	0.32	1	0.46 ± 0.02
	Medium scale	0.47 ± 0.02	0.36	3	0.42 ± 0.02
	Low scale	0.52 ± 0.02	0.41	5	0.39 ± 0.01
Slot texture (Tx_S)	High scale	0.44 ± 0.01	0.40	1	0.44 ± 0.01
	Medium scale	0.40 ± 0.01	0.36	3	0.40 ± 0.01
	Low scale	0.51 ± 0.02	0.23	3	0.29 ± 0.01

Table 4 summarizes the results of the tribological tests in terms of the initial slope of the traction coefficient curve, the value where the COT is saturated and the respective value of the slip percentage at which total slip occurred in the rail-wheel contact region for the different textures evaluated [62,63]. For both texture designs the traction coefficient increases for slip values below 1%, except for the low scale slots.

For both texture geometries at all scales, except for the low scale grooving, the traction coefficient increased for slip values below 1% (see Figure 9); this allows the conclusion that the texture modifies the COT at low slip percentages (≤1%).

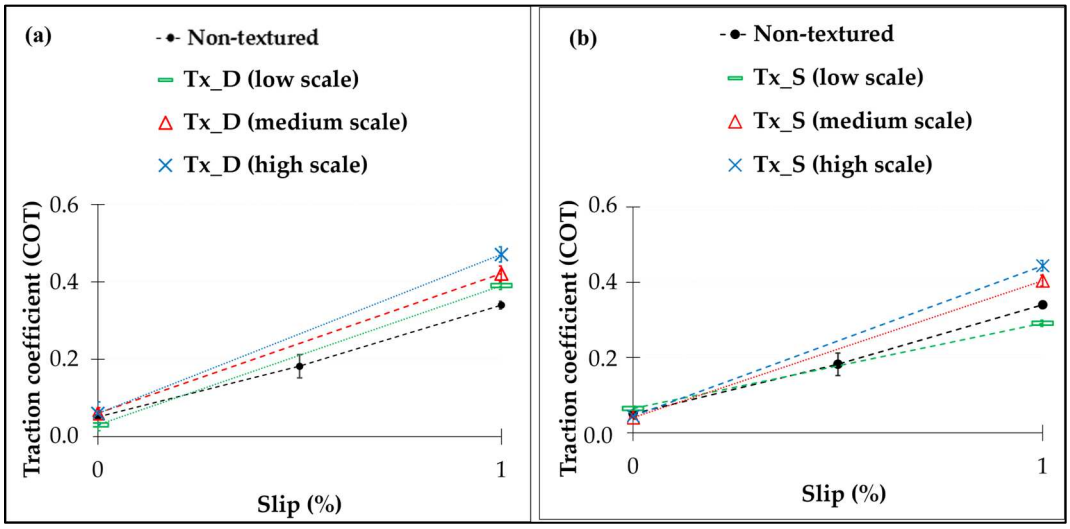


Figure 9. Variation in the coefficient of traction for 0% and 1% slip: (**a**) Diamond texture (Tx_D); (**b**) Slot texture (Tx_S).

Figure 10 shows representative traction coefficient (COT) curves over 8000 cycles for the high-scale diamond-textured and non-textured surfaces. These curves illustrate the evolution of the traction response under repeated rolling–sliding contact. The high-scale diamond-textured surface reaches friction saturation at approximately 1% slip, with a stable COT of 0.46, corresponding to its limiting coefficient of friction (COF). In contrast, the non-textured surface requires approximately 5% slip to reach saturation, with a stable COF of 0.49.

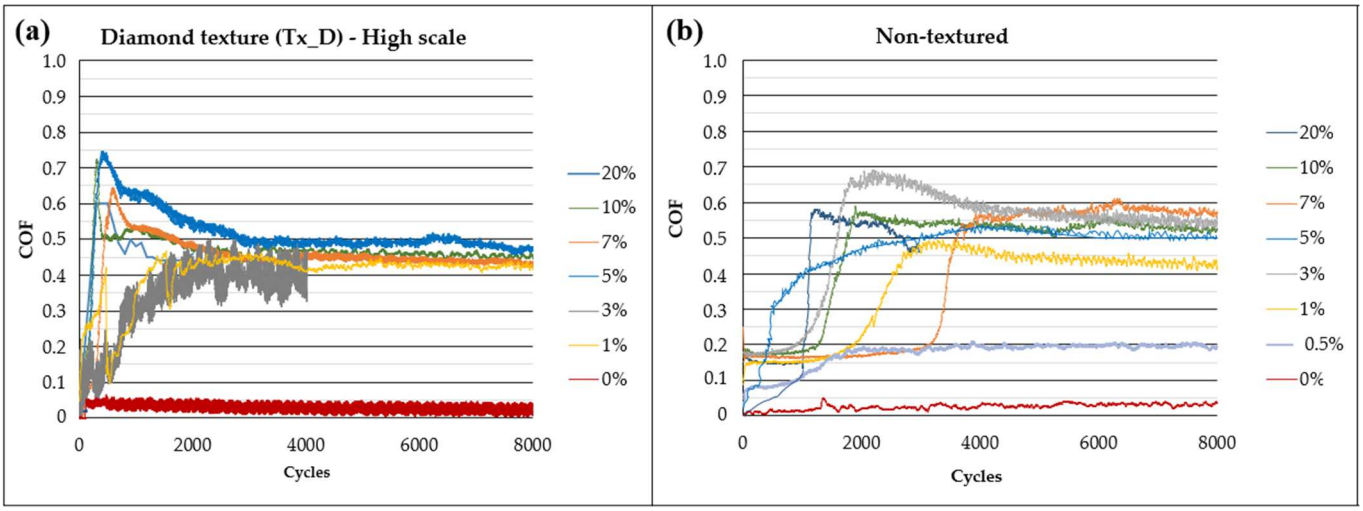


Figure 10. Comparative COF curves for: (**a**) high-scale diamond-textured and (**b**) non-textured surfaces.

3.4.2. Wear and Energy at the Contact

Figure 11 shows the wear rate as a function of the energy at the contact ($T\gamma/A$) after twin disc tests for three different pairs in contact: non-textured wheel and rail discs, non-textured wheel disc versus diamond textured rail disc (high scale), and non-textured wheel disc versus slot textured rail disc (low scale). When the slip ratio was increased to 20% the $T\gamma/A$ value reached approximately 90 N/mm^2 for untextured surfaces in contact. When samples with diamond texture were tested, however, the maximum $T\gamma/A$ value reached was 29 N/mm^2 (also for 20% slip) due to an effective reduction in the projected

contact area. This was, in fact, the only testing condition that led to a catastrophic wear regime of the diamond-textured surfaces.

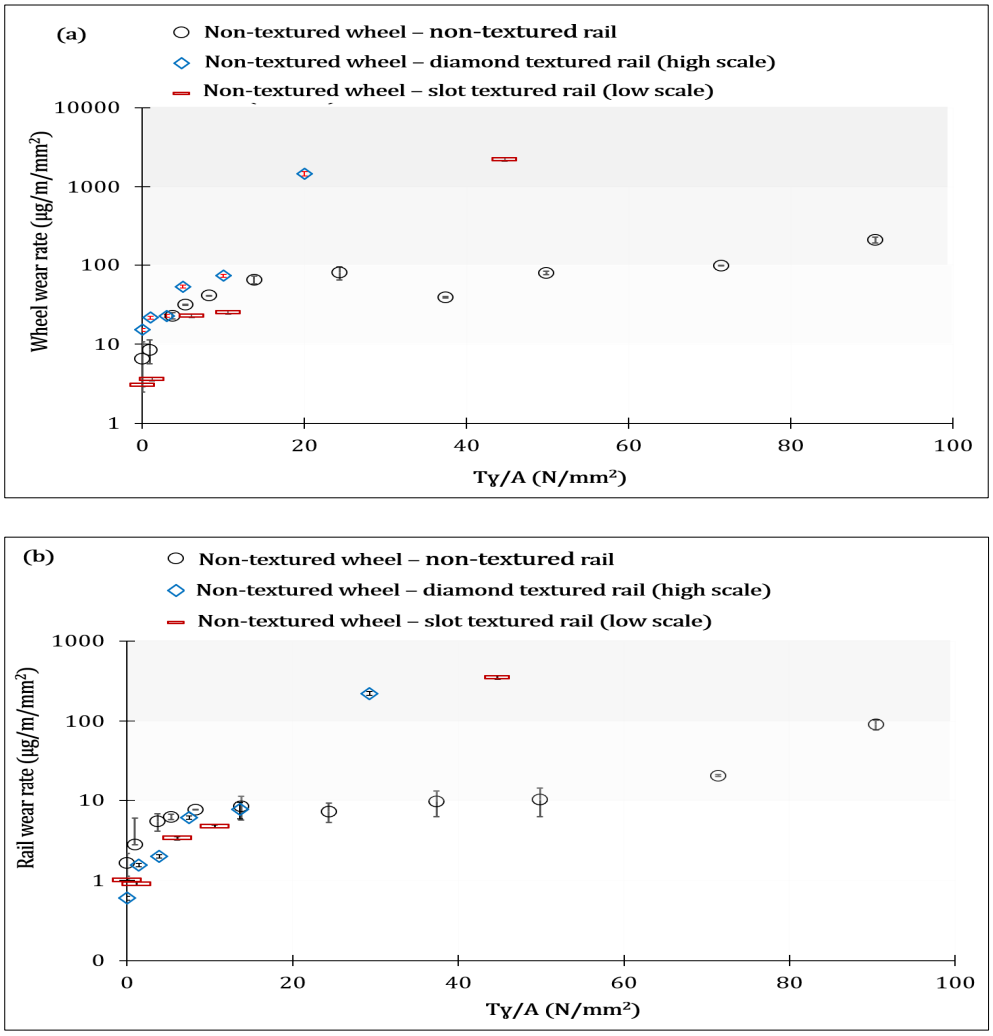


Figure 11. Wear rate versus Energy at the contact—$T\gamma$ approach: (**a**) Wheel samples, (**b**) Rail samples.

The behaviour discussed above, correlates well with the mechanism of rolling contact fatigue (RCF) of the surfaces. For instance, for 1% slip, there was a reduction in the mean crack angle, length of cracks, depth of the deformed layer and, (see Figure 12 and Table 5) also a decrease in the contact stresses (see Table 6). For the slot texture the contact stresses are large at the edges of the grooves, which causes significant plastic deformation in localized regions and an increase in the wear rate as well. These larger, localized wear rates help control the intensity of RCF since they are responsible for the detachment of surface layers containing fatigue cracks when they are still incipient.

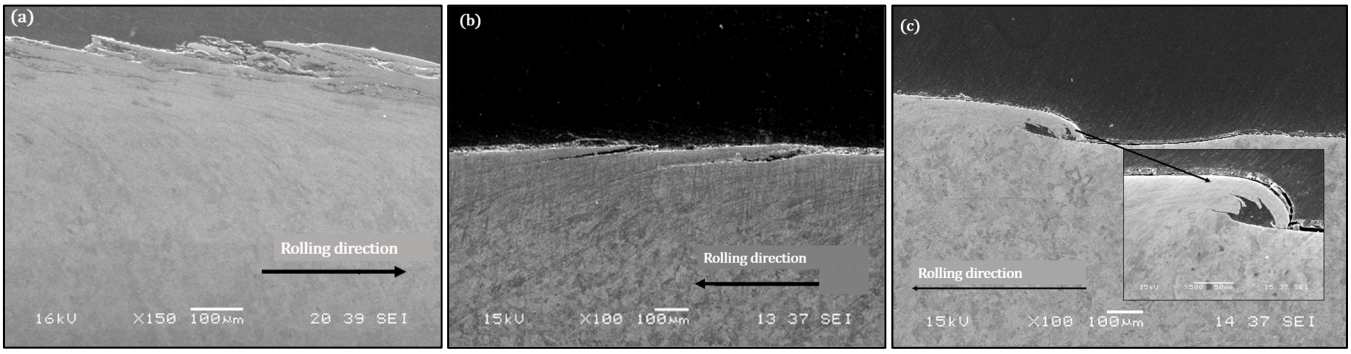


Figure 12. Cross-sectional view of R400HT rail samples after twin disc tests with 1% slip in contact with untextured E8 wheel samples (the arrow shows the rolling direction): (**a**) Untextured sample; (**b**) Diamond texture; (**c**) Slot texture.

Table 5. Crack measurement and depth of deformed layer for R400HT rail with 1% slip.

		Non textured	Diamond-D (Rail), High Scale	Slot-S (Rail), Low Scale
Crack length (µm)	**Rail**	569 ± 85	467 ± 18	467 ± 20
Crack angle (°)	**Rail**	8.5 ± 1.3	4.1 ± 0.6	6.8 ± 0.5
Depth of deformed layer (µm)	**Rail**	408 ± 15	220 ± 20	38 ± 22
	Wheel	409 ± 15	201 ± 28	313 ± 50

Table 6. Contact stress calculation.

Contact Stress		Non-Textured	Diamond-D (Rail)	Slot-S (Rail)
Normal maximum stress (GPa)	σ_{xmax}	−1.3	−0.42	−0.94
	σ_{ymax}	−1.3	−0.42	−0.94
	σ_{zmax}	−0.78	−0.25	−0.56
Maximum shear stress (GPa)	$\tau_{1,max}$	0.4	0.13	0.28
Depth of Maximum shear stress is location in the z-axis (µm)	$z_{\tau_{1,max,}}$	211.36	715.26	298.68

Table 5 summarizes the main results of the tests with 1% slip. The decrease in RCF in the rail discs was confirmed by measuring the angle and length of the cracks and was also demonstrated by the decrease in the thickness of the deformation layer for both discs.

3.4.3. Experimental Contact Width

Figure 13 presents representative contact patterns obtained using Fuji Prescale pressure-sensitive film for non-textured and deterministically textured surfaces with different geometries and scales. The corresponding predicted and experimentally measured modified contact semi-widths (a*) are summarized in Table 7, distinguishing the contact configurations with and without the interposed film. The results show that the diamond-textured configuration exhibits a greater apparent contact semi-width than the non-textured surface, demonstrating the influence of deterministic texture geometry on the contact dimensions.

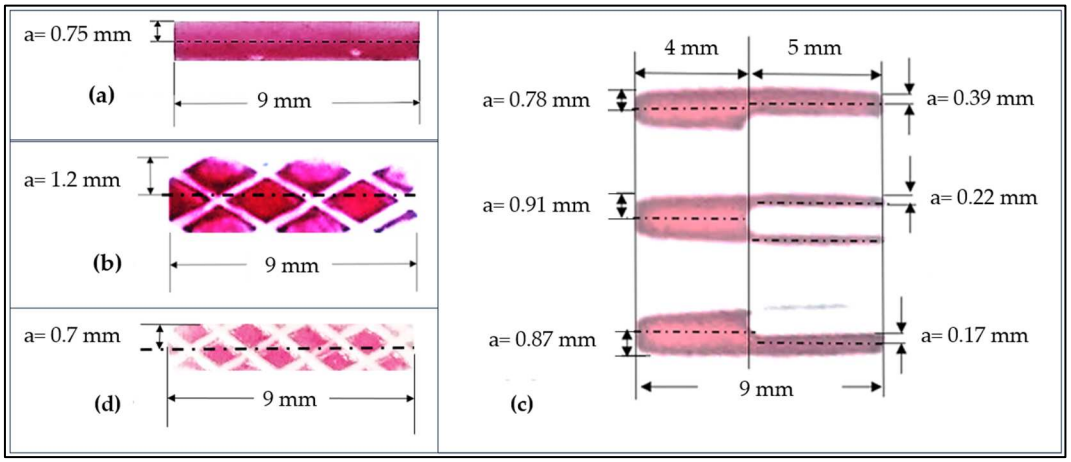


Figure 13. Contact semi-width measurements for different contact conditions and textures: (**a**) Non-textured; (**b**) D: Diamond texture; (**c**) S: Slot texture, (**d**) LD: Low scale diamond texture (l = 1.0 mm, w = 0.7 mm, λ = 0.8 mm).

Table 7. Comparison of predicted and experimentally measured modified contact semi-widths a* for different surface configurations, with and without pressure-sensitive film.

Surface Configuration	Predicted Mean Without Film (mm)	Predicted Mean with Film (mm)	Experimental Mean with Film (mm)
(a) Non-textured	0.28	0.77 ± 0.10	0.75 ± 0.05
(b) Diamond texture	0.91 ± 0.28	0.95 ± 0.30	1.20 ± 0.31
(c) Slot texture	0.39 ± 0.35	0.49 ± 0.32	0.48 ± 0.36
(d) Low-scale diamond texture	0.45 ± 0.11	0.55 ± 0.13	0.70 ± 0.15

As established in the previous section, the contact semi-width depends on the design, scale, and spatial distribution of the texture elements. Although the nominal contact length corresponds to the cylinder width (L = 9 mm), the effective contact length varies according to the position of the contact line within the deterministic pattern. Consequently, under the same applied normal load and material properties, variations in the effective contact length modify the contact semi-width and the resulting pressure distribution, as described by the modified Hertzian formulation.

Table 7 provides a quantitative comparison between the predicted and experimental values. For the diamond-textured configuration, the predicted mean contact semi-width was 0.91 ± 0.28 mm without the film and 0.95 ± 0.30 mm with the film, whereas the experimentally measured mean value was 1.20 ± 0.31 mm. The differences between predicted and experimental values must be interpreted considering the additional compliance introduced by the pressure-sensitive film and the assumptions of the analytical contact model.

It should be noted that the experimental measurements were performed using a viscoelastic film, whereas the adapted Hertz model assumes elastic contact between homogeneous solids. As a consequence, the measured contact widths are systematically larger than those predicted by the Hertzian approach. This difference is expected and arises from the additional compliance of the viscoelastic layer, which increases the apparent contact area under load.

3.4.4. Numerical Contact Width

The contact areas obtained from the finite element simulations were quantified using ImageJ image analysis software (version 1.XX; National Institutes of Health, Bethesda, MD, USA). For the textured configuration, the individual load-bearing contact regions

were identified and their areas measured and summed to determine the total effective contact area. The results showed that the total calculated contact area remained nearly constant, changing from 4.95 ± 0.01 mm² for the non-textured configuration to 5.13 ± 0.01 mm² for the diamond-textured configuration, whereas the apparent contact width increased from 0.56 ± 0.01 mm to 0.66 ± 0.01 mm, respectively (Figure 14a).

The variability with respect to the theoretical reference was approximately 3%, demonstrating that surface texturing effectively increases the contact width without significantly altering the real contact area, although the apparent contact area increased by approximately 20%.

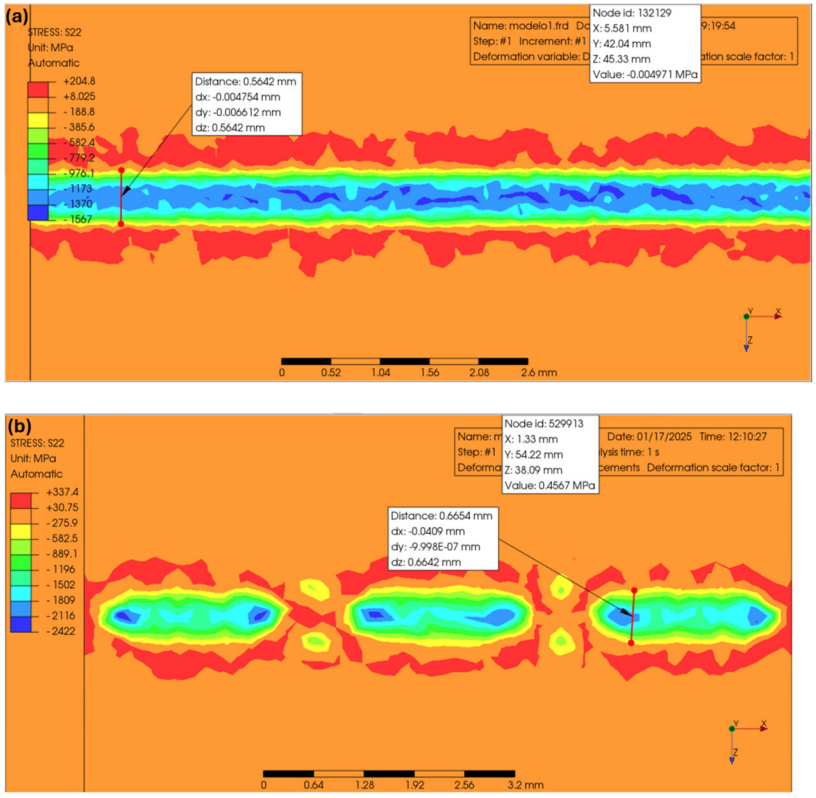
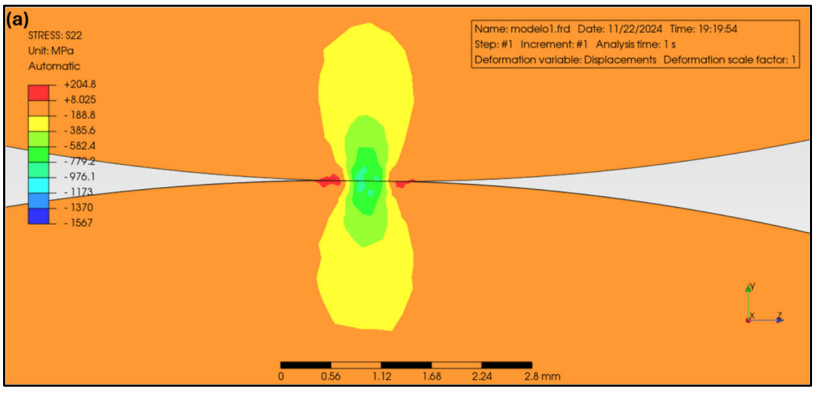


Figure 14. Contact width: (**a**) Non-textured contact configuration; (**b**) D: Diamond texture.

The contact pressure distributions for both untextured (Figure 15a) and textured (Figure 15b) surfaces are shown in Figure 15. A noticeable reduction in contact pressure is observed for the textured surface, which supports the theoretical calculations obtained from the modified Hertzian contact model incorporating surface texture effects (see Figure A4).



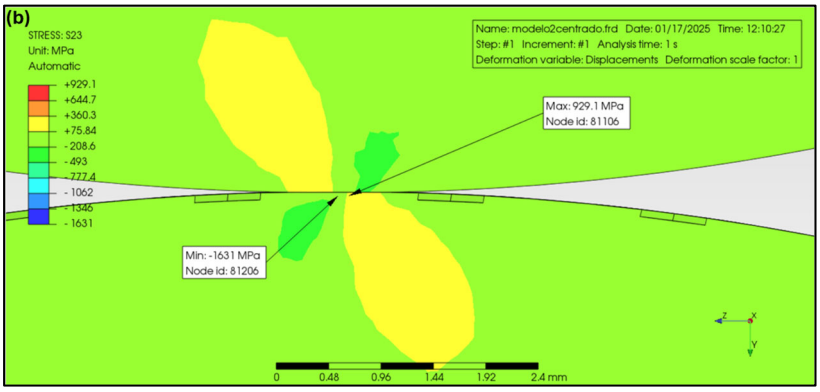


Figure 15. Contact pressure contact width: (**a**) Non-textured; (**b**) D: Diamond texture.

3.4.5. Proposed Mechanical Contact Behaviour Under Rolling–Sliding Conditions

It was found that the contact semi-width increased in the textured discs, which led to a reduction in the apparent contact pressure and subsequent effects on the stick/slip ratio for each percentage of slip. The model developed can be used to predict the coefficient of traction under rolling–sliding conditions as a function of the deterministic pattern designed. Also, it shows that it is possible to reach a constant friction condition in textured surfaces at lower slip percentages when compared to stochastic surfaces. This is a benefit in problems such where friction control is difficult, e.g., in contacts with a low slip percentage a texture can be designed to increase the COT or in cases where the slip percentage is higher than 5% it can be modified as required.

Figure 16 shows the analytical relationship between the apparent contact semi-width (a_{L_T}) and the stable coefficient of friction, fitted to experimental data from 15 texture configurations tested in five replicas each. The contact semi-width is governed by the texture geometry: for a given texture angle, each contact line crosses a number (n_j) of diamond elements of equal projected length L_i, so that the total contact length is obtained by summing all L_T contributions across all pattern rows (n_j) crossing the contact (Equation 1, Figure 4). This geometric formulation, grounded in Hertzian contact theory for elastic cylinders under partial slip [1,52,53] is described in detail in Section 3 and the Appendix A. The resulting model yields a third-order polynomial fit ($R^2 = 1.0$) that enables the prediction of the stable COF directly from the texture design parameters, without requiring iterative tribological testing.

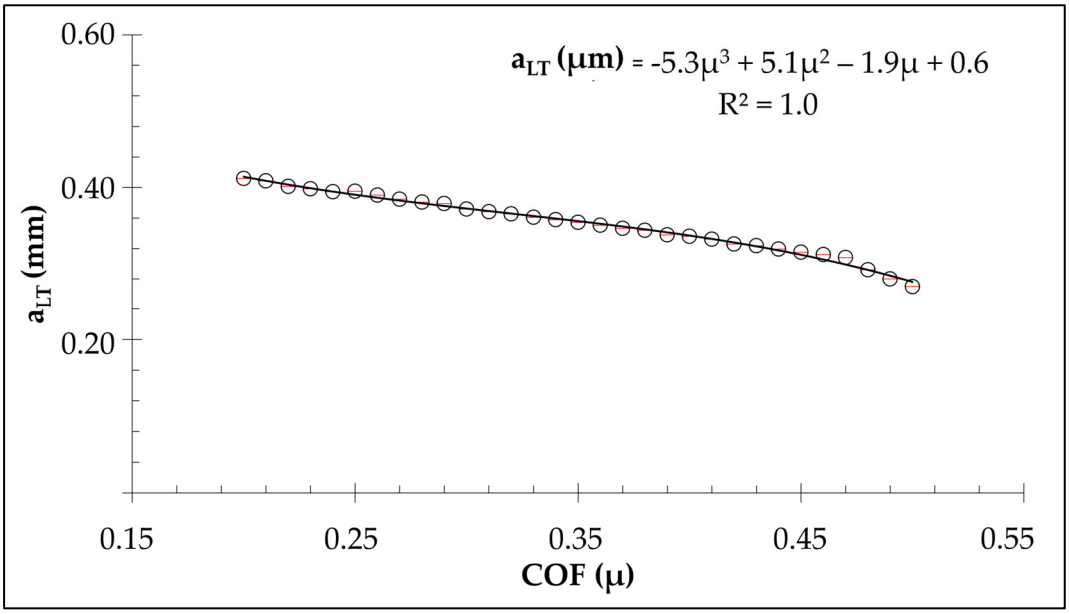


Figure 16. Contact semi-width (a_{L_T}) as a function of the coefficient of friction for 400HT rail in contact with E8 wheel.

$$L_T(\alpha_{tx}) = \sum n_j L_{i_{P_j}} \leq L, \alpha_{i_{tx}} \leq \alpha_{tx} \leq \alpha_{f_{tx}} \quad (1)$$

When the area of the textured surface $A_{ts}(x)$, is smaller than the required contact area $A_T(x)$, the value of the contact semi-width (a_{L_T}) is modified to equal the value of A_T, by a value a^*, and thus the Hertz contact equations are modified according to the texture design (for a full development of the model see the Appendix A).

$$If\ A_{ts}(x) > A_T(x), then\ a_{L_T}(x) = a^*(x), -a_{L_T} \leq x \leq a_{L_T} \quad (2)$$

The texture geometry is incorporated along each contact line, following the Hertzian line contact approach. The number of texture elements intersected by the contact line and their corresponding projected lengths determine the effective contact length, which is used to calculate the available contact area and the modified contact semi-width. Therefore, no additional shape factor is required, since the geometrical characteristics of the deterministic texture are already explicitly considered in the formulation.

Then, it is possible to define a projected texturized area A_p:

$$A_p(x) = 2a^*(x)L_T(x) \quad (3)$$

The volumetric wear rate is given by:

$$V_{wr} = \frac{A_p * \Delta h}{distance\ run} \quad (4)$$

Using the volumetric wear rate is possible to deduce the equation of energy density or energy per unit volume, which is written as:

$$Energy\ per\ unit\ volume = \frac{T\gamma(\mathrm{N})}{V_{wr}(\mathrm{m^3/m})} \quad (5)$$

where h is the height of texture elements, T is the tangential force at the contact surface, and γ is the slip ratio.

The stable coefficient of friction (COF) decreased for the high- and medium-scale diamond and slot textures and increased for the low-scale textures (Table 4). This is due to the change in the contact length (L_T) and the contact semi-width (a_{L_T}) given by the texture pattern (α_{tx}) on the contact surface. However, there was a change in the COT for slip percentages lower than 5% for both textures. Texture design can be used to control this value with based on the known correlation between the slip percentage and the slip portion of the contact patch. For example, for the untextured surfaces in this work, the slip region accounts for 57% of the contact patch when the slip percentage is 1%. If it is required to modify the COT to the value where it is saturated, then a texture pattern can be designed in a way that the slip region still represents 57% of the contact patch, but the contact semi-width is adjusted accordingly. In the case of diamond texture, for instance, the average contact semi-width was greater than 0.50 mm for 1% slip.

Therefore, to guarantee that the COT will reach the stable value of 0.47 (Figure 8) a semi-width of contact must be set to approximately 0.29 mm, which corresponds to 57% of 0.5 mm (Figure 14).

4. Discussion

Surface texturing has been extensively investigated as a means of modifying friction and wear in tribological contacts. Many proposed mechanisms are associated with lubrication, where texture elements can act as lubricant reservoirs or contribute to hydrodynamic pressure generation [47,79]. However, the present investigation examines a different mechanism based on the geometrical modification of contact conditions under dry

rolling–sliding. In particular, the results indicate that deterministic textures can increase the apparent contact area while maintaining an approximately constant total load-bearing surface contact area. This distinction provides a basis for interpreting the redistribution of contact stresses and the experimentally observed reductions in subsurface damage.

Previous contact mechanics investigations provide a foundation for this interpretation. Nowell and Hills [80] examined Hertzian contact between ground surfaces and demonstrated that surface topography can increase the contact width while producing local pressure concentrations. Prodanov et al. [53] also investigated contact mechanics in laser-textured surfaces, establishing the relevance of texture geometry to contact conditions. These investigations demonstrate that the spatial distribution of surface features influences the mechanical response of a contact. In the present study, the use of deterministic textures with controlled geometrical dimensions allows the apparent contact region to be modified while maintaining the analytical framework of elastic Hertzian contact. Nevertheless, local plastic deformation may occur under sufficiently high contact stresses, and the applicability of this interpretation depends on the relationship between texture dimensions, applied load, and material properties.

The distinction between apparent and actual surface contact area is particularly important. For the non-textured configuration, the numerical contact width was 0.56 ± 0.01 mm. Considering a contact length of 9 mm, the corresponding apparent contact area was 5.04 mm^2. For the diamond-textured configuration, the contact width increased to 0.66 ± 0.01 mm, corresponding to an apparent contact area of 5.94 mm^2. Thus, deterministic texturing increased the apparent contact area by approximately 18%. However, the total surface contact area obtained by measuring and summing the individual load-bearing contact regions from the finite element results using ImageJ remained nearly constant: 4.95 ± 0.01 mm^2 for the non-textured surface and 5.13 ± 0.01 mm^2 for the diamond-textured surface. This represents an increase of only approximately 3.6%. These results demonstrate that the increase in apparent contact area does not correspond to a proportional increase in the actual surface area carrying the applied normal load.

The mechanical significance of this result is that the deterministic texture distributes the load-bearing contact regions over a wider apparent contact area. At the surface, the applied load is transmitted through separated contact regions, whereas beneath the surface the stress fields generated by these regions extend and superimpose within the continuous material. Consequently, the increased apparent contact width modifies the spatial distribution of stresses beneath the surface, potentially reducing certain stress concentrations and contributing to a more favourable subsurface mechanical response. The finite element results support this interpretation through the calculated changes in contact stresses under static normal elastic loading. This mechanism is distinct from a simple increase in the actual surface contact area: the proposed benefit arises from the geometrical redistribution of the load-bearing regions and their associated subsurface stress fields.

This interpretation may also contribute to understanding why deterministic texturing has produced favourable wear behaviour in previous experimental investigations. Studies conducted under dry sliding conditions have demonstrated that surface texture geometry can modify friction and wear, sometimes improving wear resistance without a corresponding reduction in the coefficient of friction. Gachot et al. [54] investigated the effects of texture alignment and geometrical characteristics on dry friction, whereas Xing et al. [81] reported improved wear resistance despite increased friction in laser-textured ceramic surfaces. Other investigations have demonstrated the influence of asymmetric texture geometry on dry friction [82] and changes in wear behaviour in textured cemented carbides [83]. Although these investigations involve different materials and predominantly pure sliding contacts, their findings are consistent with the broader hypothesis that improvements in wear resistance may involve changes in contact mechanics rather than

depending exclusively on friction reduction. The present results provide an additional mechanical interpretation of this possibility through the distinction between actual surface contact area and apparent contact geometry. However, the specific mechanisms operating in these earlier studies cannot be established solely from the present analysis.

The manufacturing process must also be considered when interpreting the experimental results. The modified Hertzian contact model and the static linear-elastic FEM describe the geometrical contribution to contact width, area, and stress distribution without incorporating the localized work hardening induced by the manufacturing process.

The diamond texture produced by knurling exhibits localized work hardening in the textured valleys, with hardness values of approximately 580 ± 10 HV compared with 404 ± 10 HV on the contact surface. Such local changes in material properties may influence the wear and fatigue response. Nevertheless, the CNC-machined slot texture, which exhibits an approximately uniform hardness of 402 ± 10 HV, also demonstrates beneficial tribological behaviour. The results of both texture types are therefore consistent with an important contribution from contact geometry, although they do not completely exclude the influence of manufacturing-induced metallurgical changes. The geometrical and material contributions should be further separated in future investigations.

According to Carter's creepage theory, the development of tangential force in rolling–sliding contacts depends on contact conditions and the relationship between adhesion and slip within the contact region [51,53,84]. The initial slope of the traction–creepage curve can also be influenced by surface roughness and the associated contact geometry [67,73,74]. Therefore, modifications in the apparent contact dimensions may influence the development and saturation of tangential forces. The experimental results of the present investigation demonstrate that deterministic surface textures modify the coefficient of traction (COT) and can produce friction saturation at lower slip percentages than those observed for the non-textured configuration. The geometrical–analytical correlation presented in Figure 16 further examines the relationship between apparent contact semi-width and the experimentally measured stable coefficient of friction (COF). This correlation includes 15 texture configurations, incorporating the six initial geometries reported in Table 3, and supports the experimentally observed relationship between texture geometry and friction response within the investigated conditions.

However, the modification of friction should not be interpreted as the only explanation for changes in wear. The present experimental results demonstrate reductions in subsurface damage for selected textured configurations. At 1% slip, the mean crack length decreased from 569 ± 85 μm for the non-textured configuration to 467 ± 18 μm for the diamond texture and 467 ± 20 μm for the slot texture. Similarly, the depth of the heavily deformed layer decreased from 408 ± 15 μm to 220 ± 20 μm and 38 ± 22 μm, respectively. These results are consistent with the proposed contribution of contact stress redistribution to the mechanical response beneath the surface. In this interpretation, a wider apparent contact region may favourably modify the distribution of subsurface normal and shear stresses, reducing the conditions associated with accumulated deformation and rolling contact fatigue. Nevertheless, the static finite element model does not directly simulate cyclic shear loading, plastic deformation, crack propagation, or wear; therefore, these experimental observations support the proposed mechanism without constituting a direct numerical validation of the complete damage process.

An important difference between the present investigation and much of the previous experimental literature is the contact kinematics. Many surface-texturing studies have evaluated dry pure sliding conditions, whereas the present investigation considers dry rolling–sliding contacts over a range of slip percentages. This distinction is especially relevant when interpreting the relationship between frictional energy dissipation and wear. The $T\gamma/A$ analysis allows the wear response to be examined in relation to frictional energy

dissipation as slip increases. At high slip percentages, particularly under the severe conditions investigated, the contact can enter a substantially different wear regime associated with increased energy dissipation. The catastrophic wear observed for the high-scale diamond texture at 20% slip must therefore be distinguished from the lower-slip conditions in which beneficial effects on wear-related damage were obtained. High-slip conditions may be relevant to severe braking-related or reduced-adhesion situations in railway operation, although the twin-disc tests do not reproduce all the mechanical and thermal characteristics of an actual braking event. The occurrence of catastrophic wear under these conditions does not invalidate the geometrical contact mechanism; rather, it indicates that slip-dependent energy dissipation and the associated wear regime must be considered separately from the static normal contact response.

Taken together, the analytical, numerical, and experimental results support the interpretation that deterministic texturing can modify the mechanical response of dry rolling–sliding contacts by increasing the apparent contact area without substantially increasing the total load-bearing surface contact area. The redistribution of the contact regions over a wider apparent area modifies the subsurface stress field and provides a plausible mechanical contribution to the experimentally observed reductions in deformation and rolling contact fatigue damage. This interpretation is compatible with previous dry-contact studies reporting beneficial wear behaviour in textured surfaces, including cases in which friction does not decrease. However, its applicability to other materials, texture scales, and loading conditions requires further validation. The influence of lubrication on the proposed geometrical contact mechanism is also a relevant subject for future investigation.

From an engineering perspective, deterministic surface texturing may offer a geometrical approach to controlling friction and wear in railway wheel–rail contacts. Nevertheless, the translation of the present twin-disc findings to operational railway systems requires additional research into texture durability, manufacturing costs, long-term wear evolution, and thermomechanical effects at high slip. These aspects are necessary to establish whether the proposed contact geometry can provide sustained tribological benefits under service conditions.

The experimental tests included up to 8000 rolling–sliding cycles, allowing the tribological response of the textured surfaces to be evaluated under repeated loading (Figure 10). The deterministic texture patterns remained visually identifiable in the specimens examined after testing. However, this qualitative observation does not constitute a quantitative assessment of texture durability, since post-test profilometric measurements of texture dimensions were not performed. Furthermore, the increased wear observed at 20% slip demonstrates that texture preservation and tribological performance depend on operating conditions. Additional investigations are therefore required to quantify progressive texture degradation and establish long-term durability under representative railway service conditions.

5. Conclusions

The main conclusions of this investigation are as follows:

1. Contact geometry and load-bearing area. The modified Hertzian contact model, supported by static finite element analysis and experimental contact-width measurements, demonstrated that deterministic surface texturing modifies the apparent contact geometry under normal loading. For the high-scale diamond texture, the apparent contact width increased from 0.56 ± 0.01 mm to 0.66 ± 0.01 mm, representing an increase of approximately 18%. The corresponding apparent contact area increased from 5.04 to 5.94 mm^2, while the total load-bearing surface contact area represented in the FEM increased by only 3.6%, from 4.95 ± 0.01 to 5.13 ± 0.01 mm^2. These results

support the initial geometrical hypothesis that deterministic textures redistribute the contact regions over a wider apparent area.

2. Contact stress redistribution. The analytical maximum normal contact stress decreased from 1.30 GPa for the non-textured configuration to 0.42 GPa for the diamond texture and 0.94 GPa for the slot texture, corresponding to reductions of approximately 68% and 28%, respectively. These changes demonstrate the influence of texture geometry and effective contact length on the calculated contact stresses. The static linear-elastic FEM further supported the geometrical contact analysis, without simulating cyclic plastic deformation or wear.
3. Traction response under low-slip rolling–sliding conditions. At 1% slip, the high-scale diamond texture increased the coefficient of traction (COT) from 0.34 ± 0.01 to 0.46 ± 0.02, representing an increase of approximately 35%. Friction saturation was reached at approximately 1% slip, compared with 5% for the non-textured configuration, while maintaining a comparable stable coefficient of friction (COF) of 0.46 versus 0.49. This finding is particularly relevant to the potential application of deterministic surface textures as geometry-based dry friction modifiers in wheel–rail contacts requiring enhanced traction at low creepage.
4. Subsurface deformation and rolling contact fatigue damage. At 1% slip, the mean crack length in the rail samples decreased from 569 ± 85 μm to approximately 467 μm for the selected diamond and slot textures, corresponding to a reduction of approximately 18%. The depth of the heavily deformed layer decreased from 408 ± 15 μm to 220 ± 20 μm for the diamond texture and 38 ± 22 μm for the slot texture, representing reductions of approximately 46% and 91%, respectively. These experimental results are consistent with a beneficial contribution from the redistribution of contact stresses, although the relative effects of geometry and manufacturing-induced work hardening cannot be fully quantified.
5. Operating conditions and wear regimes. The experimental results showed that the tribological benefits of deterministic texturing depend on texture geometry and slip conditions and cannot be generalized to the entire operating range. Although enhanced traction was obtained under selected low-slip conditions, the high-scale diamond texture exhibited substantially increased wear at 20% slip. This behaviour must be interpreted within the established wheel–rail wear-regime framework, since transitions to catastrophic wear have also been documented for non-textured R400HT–E8 contacts [57,85]. The $T\gamma/A$ approach provides a basis for interpreting the relationship between operating conditions and wear response, supporting the identification of suitable texture and material combinations. Therefore, the results support the proposed geometrical contact mechanism while demonstrating that potential railway applications must be assessed according to the relevant traction requirements and wear regimes.

Overall, the results support the initial geometrical hypothesis and demonstrate the potential of deterministic surface texturing as a dry friction management approach, particularly under low-creepage rolling–sliding conditions. However, its practical applicability depends on the operating conditions and associated wear regimes, highlighting the importance of $T\gamma/A$ wear maps for guiding texture and material selection.

Author Contributions: P.A.C.: Conceptualization; Data curation; Formal analysis; Investigation; Methodology; Software; Validation; Substantial contribution to the concept or design of the work, acquisition, analysis or interpretation of data, Drafted the article. Finite element analysis; Methodology; Validation; Analysis and interpretation of simulation results; Writing—review and editing. A.T.: Revised it critically for important intellectual content, Supervision, Writing—review and editing. J.M.M.: Revised it critically for important intellectual content, Validation; Approved the version

to be published, Resources, Writing—review and editing. R.L.: Supervision, Validation; Revised it critically for important intellectual content, Drafted the article, Writing—review and editing; Approved the version to be published. L.H.M.: Numerical modelling; Finite element analysis, interpretation of simulation result. All authors have read and agreed to the published version of the manuscript.

Funding: This work was supported by Minciencias-Colombia, project No. 197-2019, and by the Vice-Rectory for Research and Extension (VIE) of the Universidad Industrial de Santander through project No. 4268, "Tribological modelling using the Archard model for a wear system to assess integrity in maintenance management.".

Data Availability Statement: The data that support the findings of this study are available from the corresponding author upon reasonable request.

Acknowledgments: The authors are grateful to Metro de Medellín for providing the rail and wheel materials used in this study.

Conflicts of Interest: The authors declare that they have no known competing financial interests or personal relationships that could have appeared to influence the work reported in this paper.

Nomenclature

a	contact semi-width (mm)
$\boldsymbol{a_{L_i}}$	contact length semi-width for each $\boldsymbol{L_i}$ (mm)
$\boldsymbol{a_{L_T}}$	contact width over the line of contact (mm)
a^*	modified contact semi-width (mm)
A_p	projected texturized area (mm^2)
A_T	total apparent contact area (mm^2)
A_{ts}	area of the textured surface (mm^2)
COT	Coefficient of Traction
E8	standard wheel material
$\boldsymbol{E^*}$	effective modulus of elasticity (GPa)
F	load (N)
$\boldsymbol{F_i}$	load on each spot (N)
$\boldsymbol{F_T}$	total normal load throughout the contact length (N)
$\boldsymbol{F_T}^*$	the apparent semi-prism volume (N)
L	length (mm)
$\boldsymbol{L_i}$	contact lengths in each texture element (mm)
$\boldsymbol{L_T}$	contact length (the sum of the contact lengths in each texture element $\boldsymbol{L_i}$) (mm)
l	width of the texture element (mm)
n	number of spots the contact line passes through
P	contact pressure (GPa)
$p(x)$	semi-ellipsoidal pressure distribution (GPa)
$\boldsymbol{P_{a_{LT}max}}$	the maximum pressure (GPa)
P_j	denote each pattern of the texture
P_{max}	maximum contact pressure (GPa)
$\boldsymbol{P_{p_max}}$	the projected contact pressure (GPa)
$\overline{\boldsymbol{P^*}}$	the apparent mean contact pressure (GPa)
$\boldsymbol{P^*_{max}}$	apparent maximum contact pressure (GPa)
$\boldsymbol{p^*(x)}$	the apparent pressure distribution (GPa)
R	reduced radius (mm)
Ra	arithmetic mean deviation of the profile (μm)
Rq	root mean square deviation of the assessed profile (μm)
Rp	maximum profile peak height (μm)
Rv	maximum profile valley depth (μm)
Rsk	skewness of the assessed profile

Rku	kurtosis of the assessed profile (sharpness of the height distribution, defined on the sampling length)
R400HT	hardened premium grade rail
T	tangential force at the contact surface (N)
$T\gamma/A$	energy dissipated in contact per unit of apparent area (N/mm²)
V_c	cutting speed (m/min)
V_{ct}	contact volume in textured surfaces, (mm³)
$\boldsymbol{V_w}$	volumetric wear (mm³)
$\boldsymbol{V_{wr}}$	volumetric wear rate (mm³/m)
w	length of the texture element (mm)
$\boldsymbol{z_{\tau_{1,max,}}}$	Localization Maximum Shear Stress (mm)
$\boldsymbol{\alpha_{tx}}$	angle interval that defines the repetition pattern of the textured surface (°)
$\boldsymbol{\alpha_{i_{tx}}}$	angle interval that starts (°)
$\boldsymbol{\alpha_{f_{tx}}}$	ends at the angle interval (°)
γ	slip (%)
λ	the separation of the texture elements, or pitch (mm)
μ	stable Coefficient of Traction
ν	Poisson's ratio of the softer material
$\boldsymbol{\tau_{1,max}}$	maximum Shear Stress (GPa)

Appendix A

The starting point to develop the contact model is the set of equations used for the contact between cylinders with a continuous length L and parallel axes of revolution, as presented in Figure A1. When applying a load F, a contact width $2a$ is produced. The figure shows the contact patch as a grey shaded area that does not present discontinuities and has a semi-ellipsoidal pressure distribution p(x). These equations were modified to consider the geometry of deterministic textures, assuming that the materials of the elements involved in the contact are homogeneous and isotropic and that the forces applied to the bodies generate only elastic deformations subject to Hooke's law in the contact zone. The forces are normal to the contact surfaces, and the contact area is small compared to the surface of the elements in contact.

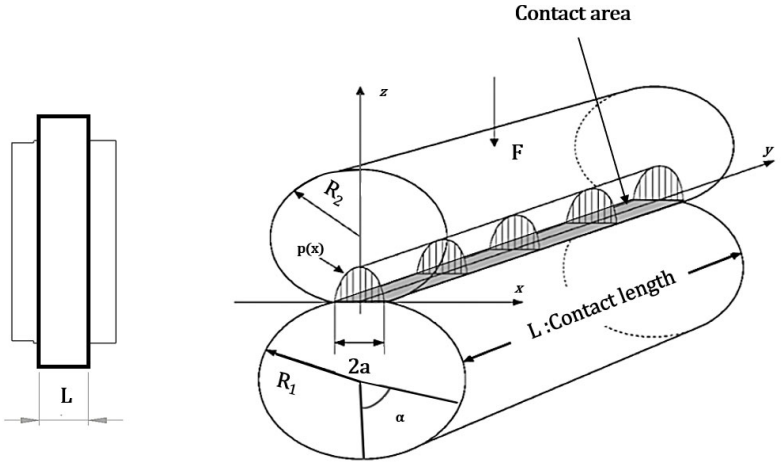


Figure A1. Hertz's line of contact. Adapted from [51].

The load onto each spot was calculated by assuming that the applied force was evenly distributed on the total length, load per unit length, and considering Equation (2) and Figure 4, so:

$$F_i(x) = \left(\frac{F}{L_T}\right) * L_i(x) \quad \text{(A1)}$$

$$F_T(x) = F \quad \text{(A2)}$$

In a cylinder–cylinder contact, a rectangular contact area is generated. However, in a textured surface, under a fixed contact load, the contact width must be increased with respect to a non-textured surface to equilibrate the stresses across the contact surface. Obviously, the other change due to texture is a variation in the contact length for each x position in the pattern. Experimental results clearly show that in textured surfaces the contact patch is still rectangular in shape. Therefore, it is assumed that the contact width remains constant over the line of contact, i.e.:

$$a_{L_T}(x) = a_{L_i}(x) \quad \text{(A3)}$$

This supposition holds for stiff materials and a short contact length as in the case under study. Accordingly, several areas can be defined: the total apparent contact area A_T, which is rectangular in shape:

$$A_T(x) = 2a_{L_T}(x)L_T(x), -a_{L_T} \le x \le a_{L_T} \quad \text{(A4)}$$

The actual total surface contact area or textured surface area A_{ts}, bounded by the diagonals of the diamonds in contact and the horizontals drawn $a_{L_T} \pm a_{L_T}$. When the area of the textured surface $A_{ts}(x)$ is less than the contact area $A_T(x)$, the value of the semi-width a_{L_T} is modified until it equals the value of A_T, at a value a^*; this can be done also using a correction factor f such that:

$$a^*(x) = f a_{L_T}(x) \rightarrow A_{ts}(x) = A_T(x) \quad \text{(A5)}$$

On the contrary, if $A_{ts}(x)$ is greater than A_T, then the obtained $A_{ts}(x)$ value is used. In other words:

$$If\ A_{ts}(x) > A_T(x), then\ a_{L_T}(x) = a^*(x), -a_{L_T} \le x \le a_{L_T} \quad \text{(A6)}$$

Then, it is possible to define a projected texturized area A_p:

$$A_p(x) = 2a^*(x)L_T(x) \quad \text{(A7)}$$

And the maximum projected area is given by the apparent length L:

$$A_{p_max}(x) = 2a^*(x)L \quad \text{(A8)}$$

To facilitate the calculations of A_{ts}, the following procedure was developed: starting at x = 0 the accumulated geometric area bounded by the diamonds and a horizontal line drawn at a coordinate X (and also -X) is calculated. Such results are shown in Figure A2. Then, interpolation functions are generated. Thus, for any position (x) of the contact line bounded by $\pm\ a_{L_T}$, A_{ts} will be calculated as:

$$A_{ts}(x) = A_{ts}(x + a_{L_T}) - A_{ts}(x - a_{L_T}) \quad \text{(A9)}$$

For example, for contact lines positioned at x = 1 mm and a_{L_T} = 0.5 mm, and x = 0 mm and a_{L_T} = 0.3 mm, the corresponding values of the total area, $A_{ts}(1)$ and $A_{ts}(0)$ will be:

$$A_{ts}(1) = A_{ts}(1 + 0.5) - A_{ts}(1 - 0.5) = 4.99 + 1.15 = 3.84\ \text{mm}^2$$

$$A_{ts}(0) = A_{ts}(0 + 0.3) + A_{ts}(0 - 0.3) = 0.77 + 0.77 = 1.54\ \text{mm}^2$$

https://doi.org/10.3390/eng7110595

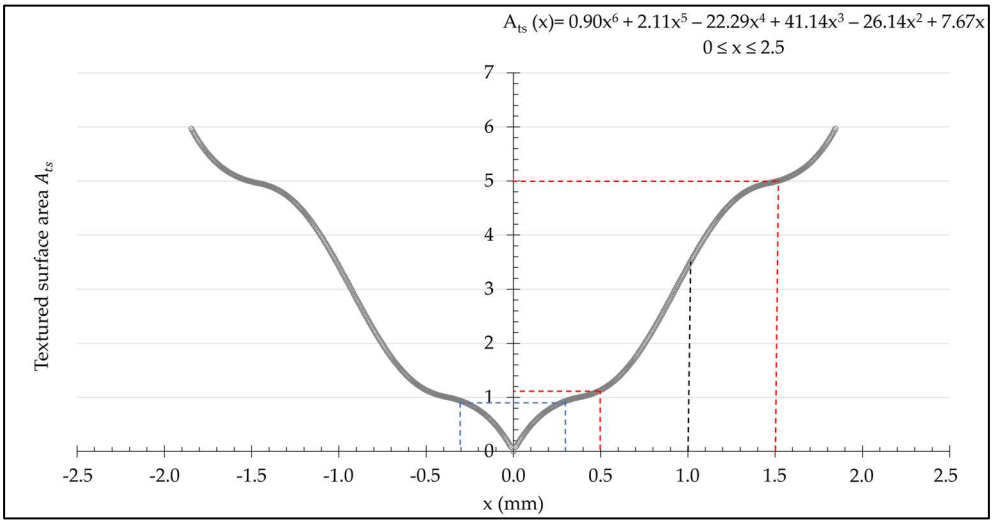


Figure A2. Accumulated textured area for the contact line positioned at x = 0 and bounded by an arbitrary x value.

Finally:

$$a_{L_i}(x) = a_{L_T}(x) = \left(\frac{4F_T(x)R}{\pi L_T(x)E^*}\right)^{\frac{1}{2}} = \left(\frac{4F_i(x)R}{\pi L_i(x)E^*}\right)^{\frac{1}{2}} \quad \text{(A10)}$$

So that:

$$a_{L_T} = \overline{a_{L_T}(x)} \quad \text{(A11)}$$

Since the contact is still cylinder on cylinder, there is a practical effect due to the texture, which is a change in the contact width. The pressure distribution will still be semi-elliptical, and it is possible to define different contact pressures. To express the contact pressure, the apparent contact area and the projected contact area is defined as shown in Figure A3.

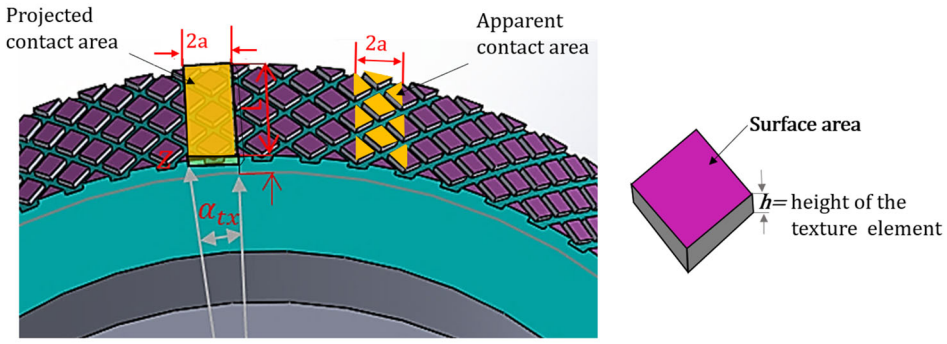


Figure A3. Definition of the different contact areas illustrated.

Equations for Contact Stresses over the Apparent Contact Area

The apparent mean contact pressure, in which the corrected contact width is used, was calculated as follows:

$$\overline{P^*}(x) = \frac{F_T(x)}{2\,a^*(x)\,L_{T(x)}} \quad \text{(A12)}$$

Although there is texture, the nature of the machined surfaces in contact is smooth, since the roughness is Ra = 0.5 μm. This will not lead to highly discontinuous contact (compared to the smooth roughness considered in Nowell & Hills) [80]), since the deterministic texture will allow for deterministic rather than stochastic pressure. And since the

texture is designed with an appropriate scale, this would not be expected to increase the stress peaks. Unlike the work of "Hertzian Contact of Ground Surfaces" which is focused on roughness and not a deterministic texture with a smooth roughness [80].

The apparent semi-prism volume is given by:

$$F_T{}^* = \overline{F_T{}^*(x)} = \frac{1}{2}\pi\, a^*(x)\, L_T\,(x) P^*{}_{max}(x) \tag{A13}$$

and the apparent maximum pressure P_{max} per each x- position is given by:

$$P^*{}_{max}(x) = \frac{F_T(x)}{\pi\, a^*(x)\, L_T(x)} \tag{A14}$$

So, the apparent mean maximum pressure is:

$$P^*{}_{max} = \overline{P^*{}_{máx}}(x)\,, \alpha_{i_{tx}} \le \alpha_{tx} \le \alpha_{f_{tx}} \tag{A15}$$

and the apparent mean pressure distribution can be expressed as:

$$p^*(x) = P^*{}_{max}\,(x)\sqrt{1-(x/a^*(x))^2}\,, -a^* \le x \le a^* \tag{A16}$$

and the maximum pressure P_{max} per each x- position is given by:

$$P_{a_{LT}max}(x) = \frac{F_T(x)}{\pi\, a_{L_T}(x)\, L_T(x)} \tag{A17}$$

Maximum Shear Stress

$$\tau_{1,max} = 0.30 P_{p_max} \tag{A18}$$

Localization Maximum Shear Stress

$$z_{\tau_{1,max,}} = 0.78\, a^* \tag{A19}$$

Equations for projected contact area

The projected average pressure

$$\overline{P_p}(x) = \frac{F_T(x)}{2a^*(x)\, L} \tag{A20}$$

Maximum projected semi-prism

$$F_T = \frac{1}{2}\pi\, a^*(x)\, L\, P_{p_max}(x) \tag{A21}$$

Maximum pressure projected per each x- position is given by,

$$P_{p_max}(x) = \frac{F_{T(x)}}{\pi a^*(x)\, L} \tag{A22}$$

Pressure distribution for any contact line

$$P_p(x) = P_{p_max}\sqrt{1-(x/a^*)^2}\,, -a^* \le x \le a^* \tag{A23}$$

"Mean" projected maximum pressure

$$P_{p_max} = \overline{P_{p_max}}(x)\,, \alpha_{i_{tx}} \le \alpha_{tx} \le \alpha_{f_{tx}} \tag{A24}$$

Due to the periodic arrangement of the deterministic texture elements, the effective contact length varies according to the position of each contact line within the geometrical pattern. These variations in effective contact length modify the contact pressures calculated using the modified Hertzian formulation under a constant applied normal load. Figure A4 presents the analytical variation in the calculated contact pressures as a function of effective contact length, while Figure A5 illustrates the corresponding pressure distributions for a representative effective contact length of 6.6 mm. These figures are part of the mathematical development of the contact model and do not represent post-test profilometric measurements.

The maximum corrected contact pressure ($P^*_{max}(x)$ Equation (A14)) for this apparent contact is shown in Figure A4, for X = 0 and P = 4905 N it has a value of 0.73 GPa. This maximum pressure is much lower than the one obtained for the same system but without texture where for 4905 N is equal to P_{max} of 1.3 GPa. The textured surfaces to compensate for the lack of material in the surface to equilibrate the applied load, increase the contact semi-width decreasing the maximum pressure. On the other hand, the maximum pressure projected ($P_{p_max}(x)$ Equation (A22)) is much lower than P^*_{max} with a value of 0.54 GPa.

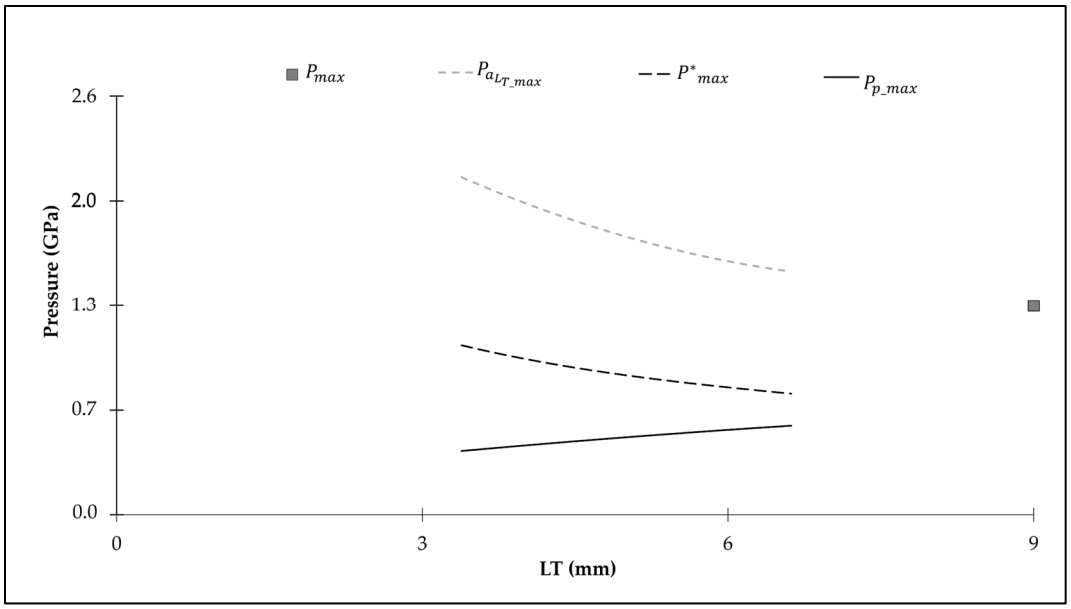


Figure A4. Maximum pressure as a function of L_T.

In view of the idealization of each body as a half-space with a plane surface, the assumptions made for each contact line (L_i) in the Hertz theory for this texture surface are as follows: (i) The surfaces are non-conforming: $a_{L_i}, a^* \ll R$; (ii) The strains are small: $a_{L_i}, a^* \ll R$; and (iii) the surfaces are friction less so that only a normal pressure is transmitted between them. It can be assumed that a state of plane strain ($\epsilon_y = 0$) is produced in the half-space by the loading line. For the assumption of plane strain to be justified the thickness of the solid should be large enough compared with the width of the loaded region.

The pressure distribution (Equations (22) and (23)) at L_T = 6.6 mm would be as illustrated below in Figure A5 the surface is continuous and has no texture there is a pressure distribution with a maximum at 1.3 GPa.

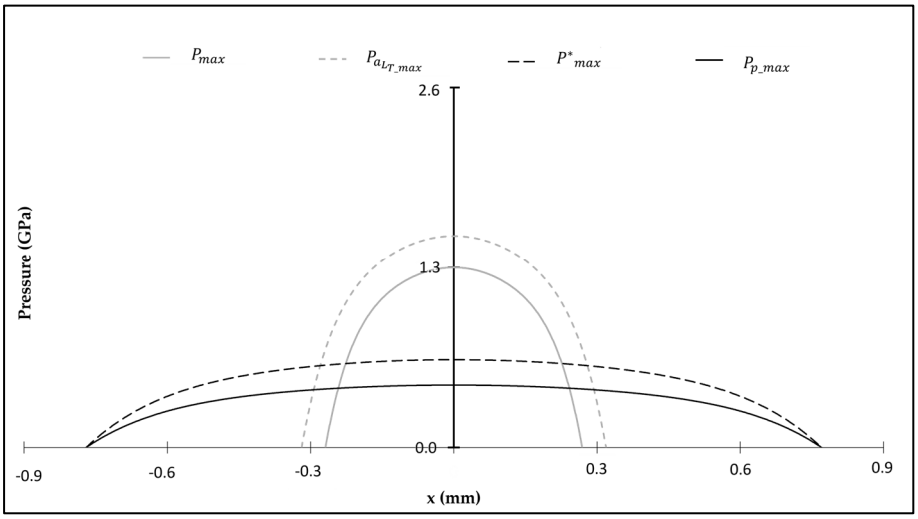


Figure A5. Pressure distribution for L_T = 6.6 mm.

References

1. Johnson, K.L. *Contact Mechanics*; Cambridge University Press: Cambridge, UK, 1985; https://doi.org/10.1017/CBO9781139171731.
2. Quost, X.; Sebes, M.; Eddhahak, A.; Ayasse, J.-B.; Chollet, H.; Gautier, P.-E.; Thouverez, F. Assessment of a semi-Hertzian method for determination of wheel–rail contact patch. *Veh. Syst. Dyn.* **2006**, *44*, 789–814. https://doi.org/10.1080/00423110600677948.
3. Hertz, H. Ueber die Berührung fester elastischer Körper. *J. Für Die Reine Und Angew. Math.* **1882**, *92*, 156–171. https://doi.org/10.1515/crll.1882.92.156.
4. Kalker, J.J. On the Rollingcontact of Two Elastic Bodies in the Presence of Dry Friction. Ph.D. Dissertation, Delft University of Technology, Delft, The Netherlands, 1967.
5. Piotrowski, J. Kalker's algorithm Fastsim solves tangential contact problems with slip-dependent friction and friction anisotropy. *Veh. Syst. Dyn.* **2010**, *48*, 869–889. https://doi.org/10.1080/00423110903178495.
6. Kalker, J.J. The Simplified Theory of Contact. In *Solid Mechanics and Its Applications*; Springer: Berlin/Heidelberg, Germany, 1990; pp. 99–135. https://doi.org/10.1007/978-94-015-7889-9_3.
7. Greenwood, J.A.; Tripp, J.H. The elastic contact of rough spheres. *J. Appl. Mech.* **1967**, *34*, 153–159. https://doi.org/10.1115/1.3607616.
8. Bush, A.W.; Gibson, R.D.; Thomas, T.R. The elastic contact of a rough surface. *Wear* **1975**, *35*, 87–111. https://doi.org/10.1016/0043-1648(75)90145-3.
9. Johnson, K.L.; Greenwood, J.A.; Higginson, J.G. The contact of elastic regular wavy surfaces. *Int. J. Mech. Sci.* **1985**, *27*, 383–396. https://doi.org/10.1016/0020-7403(85)90029-3.
10. Hu, Y.Z.; Barber, G.C.; Zhu, D. Numerical analysis for the elastic contact of real rough surfaces. *Tribol. Trans.* **1999**, *42*, 443–452. https://doi.org/10.1080/10402009908982240.
11. Zenyuk, I.V.; Kumbur, E.C.; Litster, S. Deterministic contact mechanics model applied to electrode interfaces in polymer electrolyte fuel cells and interfacial water accumulation. *J. Power Sources.* **2013**, *241*, 379–387. https://doi.org/10.1016/j.jpowsour.2013.03.165.
12. Wen, Z.; Wu, L.; Li, W.; Jin, X.; Zhu, M. Three-dimensional elastic-plastic stress analysis of wheel-rail rolling contact. *Wear* **2011**, *271*, 426–436. https://doi.org/10.1016/j.wear.2010.10.001.
13. Carbone, G. A slightly corrected Greenwood and Williamson model predicts asymptotic linearity between contact area and load. *J. Mech. Phys. Solids* **2009**, *57*, 1093–1102. https://doi.org/10.1016/j.jmps.2009.03.004.
14. Carbone, G.; Bottiglione, F. Asperity contact theories: Do they predict linearity between contact area and load? *J. Mech. Phys. Solids* **2008**, *56*, 2555–2572. https://doi.org/10.1016/j.jmps.2008.03.011.
15. Fukagai, S.; Ma, L.; Lewis, R. Tribological aspects to optimize traction coefficient during running-in period using surface texture. *Wear* **2019**, *424–425*, 223–232. https://doi.org/10.1016/j.wear.2019.02.023.
16. Greenwood, J.A.; Williamson, J.B.P. Contact of nominally flat surfaces. *Proc. R. Soc. Lond. Ser. A* **1966**, *295*, 300–319. https://doi.org/10.1098/rspa.1966.0242.

17. Holmberg, K.; Andersson, P.; Erdemir, A. Global energy consumption due to friction in passenger cars. *Tribol. Int.* **2012**, *47*, 221–234. https://doi.org/10.1016/j.triboint.2011.11.022.
18. Ripoll, M.R.; Simic, R.; Brenner, J.; Podgornik, B. Friction and lifetime of laser surface-textured and MoS2-Coated Ti 6Al4V under Dry reciprocating sliding. *Tribol. Lett.* **2013**, *51*, 261–271. https://doi.org/10.1007/s11249-013-0170-6.
19. Kikuchi, K.; Mizuno, F. Biomimetics. In *Integrated Nano-Biomechanics*; Elsevier: Amsterdam, The Netherlands, 2018.
20. Vakis, A.I.; Yastrebov, V.A.; Scheibert, J.; Nicola, L.; Dini, D.; Minfray, C.; Almqvist, A.; Paggi, M.; Lee, S.; Limbert, G.; et al. Modeling and sim-ulation in tribology across scales: An overview. *Tribol. Int.* **2018**, *125*, 169–199. https://doi.org/10.1016/j.triboint.2018.02.005.
21. Toro, A.; Abdel-Aal, H.A.; Zuluaga, E.; Cuervo, P.; Ballesteros, L.H.M.; Sánchez, J.C.; Rudas, J.S.; Isaza, C.; Misiolek, W.Z. Influence of surface morphology and internal structure on the mechanical properties and tribological response of Boa Red Tail and Python Regius snake skin. *J. Mech. Behav. Biomed. Mater.* **2021**, *119*, 104497. https://doi.org/10.1016/j.jmbbm.2021.104497.
22. Greiner, C.; Schäfer, M. Bio-inspired scale-like surface textures and their tribological properties. *Bioinspir. Biomim.* **2015**, *10*, 044001. https://doi.org/10.1088/1748-3190/10/4/044001.
23. Tzanakis, I.; Hadfield, M.; Thomas, B.; Noya, S.M.; Henshaw, I.; Austen, S. Future perspectives on sustainable tribology. *Renew. Sustain. Energy Rev.* **2012**, *16*, 4126–4140. https://doi.org/10.1016/j.rser.2012.02.064.
24. Cann, P.; Wimmer, M. Welcome to the first issue of Biotribology. *Biotribology* **2015**, *1*, 1–2. https://doi.org/10.1016/j.biotri.2015.06.001.
25. Hirano, M.; Shinjo, K. Superlubricity and frictional anisotropy. *Wear* **1993**, *168*, 121–125. https://doi.org/10.1016/0043-1648(93)90207-3.
26. Scheibert, J.; Leurent, S.; Prevost, A.; Debrégeas, G. The role of fingerprints in the coding of tactile information probed with a biomimetic sensor. *Science* **2009**, *323*, 1503–1506. https://doi.org/10.1126/science.1166467.
27. Autumn, K.; Sitti, M.; Liang, Y.A.; Peattie, A.M.; Hansen, W.R.; Sponberg, S.; Kenny, T.W.; Fearing, R.; Israelachvili, J.N.; Full, R.J. Evidence for van der Waals adhesion in gecko setae. *Proc. Natl. Acad. Sci. USA* **2002**, *99*, 12252–12256. https://doi.org/10.1073/pnas.192252799.
28. Geim, A.K.; Dubonos, S.V.; Grigorieva, I.V.; Novoselov, K.S.; Zhukov, A.A.; Shapoval, S.Y. Microfabricated adhesive mimicking gecko foot-hair. *Nat. Mater.* **2003**, *2*, 461–463. https://doi.org/10.1038/nmat917.
29. Cuervo, P.; López, D.A.; Cano, J.P.; Sánchez, J.C.; Rudas, S.; Estupiñán, H.; Toro, A.; Abdel-Aal, H.A. Development of low friction snake-inspired deterministic textured surfaces. *Surf. Topogr. Metrol. Prop.* **2016**, *4*, 1–17. https://doi.org/10.1088/2051-672X/4/2/024013.
30. Zuluaga, E.; Cuervo, P.A.; Valdés, M.; Ardila, J.G.; Rudas, J.S.; Toro, A. Energy consumption during surface texturing of AISI 1080 and AISI 52100 steels using CNC machining. *Ing. Y Compet.* **2022**, *24*, e20711301. https://doi.org/10.25100/iyc.v24i2.11301.
31. Braun, D.; Greiner, C.; Schneider, J.; Gumbsch, P. Efficiency of laser surface texturing in the reduction of friction under mixed lubrication. *Tribol. Int.* **2014**, *77*, 142–147. https://doi.org/10.1016/j.triboint.2014.04.012.
32. Tang, W.; Zhou, Y.; Zhu, H.; Yang, H. The effect of surface texturing on reducing the friction and wear of steel under lubricated sliding contact. *Appl. Surf. Sci.* **2013**, *273*, 199–204. https://doi.org/10.1016/j.apsusc.2013.02.013.
33. Gao, Y.; Sun, R.; Chen, Y.; Leopold, J. Analysis of chip morphology and surface topography in modulation assisted machining. *Int. J. Mech. Sci.* **2016**, *111*, 88–100. https://doi.org/10.1016/j.ijmecsci.2016.03.025.
34. Galda, L.; Sep, J.; Prucnal, S. The effect of dimples geometry in the sliding surface on the tribological properties under starved lubrication conditions. *Tribol. Int.* **2016**, *99*, 77–84. https://doi.org/10.1016/j.triboint.2016.03.015.
35. Oak Ridge National Laboratory. Department of Energy of U.S., 3D Printed Shelby Cobra, Energy.Gov Office of Energy Efficiency & Renewable Energy. 2015. Available online: https://www.energy.gov/eere/ammto/3d-printed-shelby-cobra (accessed on).
36. Costa, H.L.; Hutchings, I.M. Development of a maskless electrochemical texturing method. *J. Mater. Process. Technol.* **2009**, *209*, 3869–3878. https://doi.org/10.1016/j.jmatprotec.2008.09.004.
37. Michel, B.; Bernard, A.; Bietsch, A.; Delamarche, E.; Geissler, M.; Juncker, D.; Kind, H.; Renault, J.-P.; Rothuizen, H.; Schmid, H.; et al. Printing Meets Lithography: Soft Approaches to High-Resolution Patterning. *Chim. Int. J. Chem.* **2002**, *56*, 527–542. https://doi.org/10.2533/000942902777680207.
38. Bruzzone, A.; Costa, H.; Lonardo, P.; Lucca, D. Advances in engineered surfaces for functional performance. *CIRP Ann.-Manuf. Technol.* **2008**, *57*, 750–769. https://doi.org/10.1016/j.cirp.2008.09.003.

39. Myint, S.M.; Minn, M.; Yaping, R.; Satyanarayana, N.; Sinha, S.K.; Bhatia, C.S. Friction and wear durability studies on the 3D negative fingerprint and honeycomb textured SU-8 surfaces. *Tribol. Int.* **2013**, *60*, 187–197. https://doi.org/10.1016/j.triboint.2012.10.020.
40. Cazon, A.; Morer, P.; Matey, L. PolyJet technology for product prototyping: Tensile strength and surface roughness properties. *Proc. Inst. Mech. Eng. Part B J. Eng. Manuf.* **2014**, *228*, 1664–1675. https://doi.org/10.1177/0954405413518515.
41. Mann, J.B.; Guo, Y.; Saldana, C.; Yeung, H.; Compton, W.D.; Chandrasekar, S. Modulation-Assisted Machining: A New Paradigm in Material Removal Processes. *Adv. Mater. Res.* **2011**, *223*, 514–522. https://doi.org/10.4028/www.scientific.net/AMR.223.514.
42. Holmberg, K.; Erdemir, A. The impact of tribology on energy use and CO2 emission globally and in combustion engine and electric cars. *Tribol. Int.* **2019**, *135*, 389–396. https://doi.org/10.1016/j.triboint.2019.03.024.
43. Yousfi, M.; Mezghani, S.; Demirci, I.; El Mansori, M. Tribological performances of elliptic and circular texture patterns produced by innovative honing process. *Tribol. Int.* **2016**, *100*, 255–262. https://doi.org/10.1016/j.triboint.2016.01.049.
44. Shen, C.; Khonsari, M.M. The Effect of Laser Machined Pockets on the Lubrication of Piston Ring Prototypes. *Tribol. Int.* **2016**, *101*, 273–283. https://doi.org/10.1016/j.triboint.2016.04.009.
45. Usman, A.; Park, C.W. Optimizing the tribological performance of textured piston ring–liner contact for reduced frictional losses in SI engine: Warm operating conditions. *Tribol. Int.* **2016**, *99*, 224–236. https://doi.org/10.1016/j.triboint.2016.03.030.
46. Vlădescu, S.-C.; Medina, S.; Olver, A.V.; Pegg, I.G.; Reddyhoff, T. Lubricant film thickness and friction force measurements in a laser surface textured reciprocating line contact simulating the piston ring–liner pairing. *Tribol. Int.* **2016**, *98*, 317–329. https://doi.org/10.1016/j.triboint.2016.02.026.
47. Etsion, I.; Sher, E. Improving fuel efficiency with laser surface textured piston rings. *Tribol. Int.* **2009**, *42*, 542–547. https://doi.org/10.1016/j.triboint.2008.02.015.
48. Sabeur, M.; Ibrahim, D.; Mohamed, E.M.; Hassan, Z. Energy efficiency optimization of engine by frictional reduction of functional surfaces of cylinder ring–pack system. *Tribol. Int.* **2013**, *59*, 240–247. https://doi.org/10.1016/j.triboint.2012.01.015.
49. Grabon, W.; Koszela, W.; Pawlus, P.; Ochwat, S. Improving tribological behaviour of piston ring–cylinder liner frictional pair by liner surface texturing. *Tribol. Int.* **2013**, *61*, 102–108. https://doi.org/10.1016/j.triboint.2012.11.027.
50. Vencl, A.; Ivanović, L.; Stojanović, B.; Zadorozhnaya, E.; Miladinović, S.; Svoboda, P. Surface texturing for tribological applications: A review. *Proc. Eng. Sci.* **2019**, *1*, 227–239. https://doi.org/10.24874/PES01.01.029.
51. Lu, P.; Wood, R.J.K. Tribological performance of surface texturing in mechanical applications—A review. *Surf. Topogr. Metrol. Prop.* **2020**, *8*, 043001. https://doi.org/10.1088/2051-672X/abb6d0.
52. Rosenkranz, A.; Grützmacher, P.G.; Gachot, C.; Costa, H.L. Surface texturing in machine elements—A critical discussion for rolling and sliding contacts. *Adv. Eng. Mater.* **2019**, *21*, 1900194. https://doi.org/10.1002/adem.201900194.
53. Prodanov, N.; Gachot, C.; Rosenkranz, A.; Mücklich, F.; Müser, M.H. Contact mechanics of laser-textured surfaces. *Tribol. Lett.* **2013**, *50*, 41–48. https://doi.org/10.1007/s11249-012-0064-z.
54. Gachot, C.; Rosenkranz, A.; Reinert, L.; Ramos-Moore, E.; Souza, N.; Müser, M.H.; Mücklich, F. Dry friction between laser-patterned surfaces: Role of alignment, structural wavelength and surface chemistry. *Tribol. Lett.* **2013**, *49*, 193–202. https://doi.org/10.1007/s11249-012-0057-y.
55. Jiang, J.S.; Li, Q.; Liu, Q.; Kouediatouka, A.N.; Ji, H.; Dong, G. A friction mechanism for surface texturing under dry/mixed lubrication conditions based on the sublinear dependence of friction on load. *Tribol. Int.* **2024**, *194*, 109488. https://doi.org/10.1016/j.triboint.2024.109488.
56. Cuervo, P.A.; Meza, J.M.; Toro, A.; Lewis, R. Effect of surface texture on contact conditions and tribological behavior of simulated wheel–rail pairs in a twin-disc machine. In Proceedings of the 12th International Conference on Contact Mechanics and Wear of Rail/Wheel Systems (CM2022), Victoria, Australia, 4–7 September 2022; pp. 142–152.
57. Santa, J.F.; Cuervo, P.; Christoforou, P.; Harmon, M.; Beagles, A.; Toro, A.; Lewis, R. Twin disc assessment of wear regime transitions and rolling contact fatigue in R400HT–E8 pairs. *Wear* **2019**, *432–433*, 102916. https://doi.org/10.1016/j.wear.2019.05.031.
58. Lewis, R.; Olofsson, U. Basic tribology of the wheel–rail contact. In *Wheel-Rail Interface Handbook*; Lewis, R., Olofsson, U., Eds.; Woodhead Publishing, Cambridge, UK, 2009; pp. 53–56.
59. Iwnicki, S.; Björklund, S.; Enblom, R. Wheel–rail contact mechanics. In *Wheel–Rail Interface Handbook*; Lewis, R., Olofsson, U., Eds.; Elsevier: Amsterdam, The Netherlands, 2009; pp. 58–92. https://doi.org/10.1533/9781845696788.1.58.
60. Braghin, F.; Bruni, S.; Lewis, R. Railway wheel wear. In *Wheel-Rail Interface Handbook*; Woodhead Publishing, Cambridge, UK, 2009; pp. 180–182.

61. Zhu, Y.; Olofsson, U.; Söderberg, A. Adhesion modeling in the wheel-rail contact under dry and lubricated conditions using measured 3D surfaces. *Tribol. Int.* **2013**, *61*, 1–10. https://doi.org/10.1016/j.triboint.2012.11.022.
62. Stock, R.; Stanlake, L.; Hardwick, C.; Yu, M.; Eadie, D.; Lewis, R. Material concepts for top of rail friction management–Classification, characterisation and application. *Wear* **2016**, *366–367*, 225–232. https://doi.org/10.1016/j.wear.2016.05.028.
63. Fletcher, D.I.; Lewis, S. Creep curve measurement to support wear and adhesion modelling, using a continuously variable creep twin disc machine. *Wear* **2013**, *298–299*, 57–65. https://doi.org/10.1016/j.wear.2012.11.065.
64. Bucher, F.; Knothe, A.K. Theiler, Normal and tangential contact problem of surfaces with measured roughness. *Wear* **2002**, *253*, 204–218. https://doi.org/10.1016/S0043-1648(02)00102-3.
65. Polach, O. Creep forces in simulations of traction vehicles running on adhesion limit. *Wear* **2005**, *258*, 992–1000. https://doi.org/10.1016/j.wear.2004.03.046.
66. European Committee for Standardization (CEN). EN 13262; Railway applications—Wheelsets and bogies—Wheels—Product requirements. Edition/year to be confirmed.
67. Cuervo, P.; Christoforou, P.; Lewis, R.; Beagles, A.; Santa, J.F.; Toro, A. Twin disc assessment of wear regime transitions in R400ht-E8 Pairs. In Proceedings of the 11th International Conference on Contact Mechanics and Wear of Rail/Wheel Systems, CM 2018, Delft, The Netherlands, 24–27 September 2018; pp. 181–188.
68. Santa, J.F.; Christoforou, P.; Cuervo, P.A.; Toro, A.; Beagles, A.; Lewis, R. Evaluation of rolling contact fatigue of rail materials in twin disc tests. In Proceedings of the 11th International Conference on Contact Mechanics and Wear of Rail/Wheel Systems, CM 2018, Delft, The Netherlands, 24–27 September 2018; pp. 838–843.
69. *ISO 4287:1997*; Geometrical Product Specifications (GPS)—Surface Texture: Profile Method—Terms, Definitions and Surface Texture Parameters. ISO: Geneva, Switzerland, 1997. Available online: https://www.iso.org/standard/10132.html (accessed on).
70. Ballesteros, L.H.M.; Zuluaga, E.; Cuervo, P.; Rudas, J.S.; Toro, A. Tribological behavior of polymeric 3D-printed surfaces with deterministic patterns inspired in snake skin morphology. *Surf. Topogr. Metrol. Prop.* **2021**, *9*, 14002. https://doi.org/10.1088/2051-672x/abe211.
71. Persson, B.N.J.; Albohr, O.; Tartaglino, U.; Volokitin, A.I.; Tosatti, E. On the nature of surface roughness with application to contact mechanics, sealing, rubber friction and adhesion. *J. Phys. Condens. Matter* **2005**, *17*, R1–R62. https://doi.org/10.1088/0953-8984/17/1/R01.
72. Persson, B.N.; Bucher, F.; Chiaia, B. Elastic contact between randomly rough surfaces: Comparison of theory with numerical results. *Phys. Rev. B-Condens. Matter Mater. Phys.* **2002**, *65*, 1841061–1841067. https://doi.org/10.1103/PhysRevB.65.184106.
73. Greenwood, J.A.; Putignano, C.; Ciavarella, M. A Greenwood & Williamson theory for line contact. *Wear* **2011**, *270*, 332–334. https://doi.org/10.1016/j.wear.2010.11.002.
74. Ciavarella, M.; Greenwood, J.A.; Paggi, M. Inclusion of "interaction" in the Greenwood and Williamson contact theory. *Wear* **2008**, *265*, 729–734. https://doi.org/10.1016/j.wear.2008.01.019.
75. Putignano, C.; Afferrante, L.; Carbone, G.; Demelio, G. A new efficient numerical method for contact mechanics of rough surfaces. *Int. J. Solids Struct.* **2012**, *49*, 338–343. https://doi.org/10.1016/j.ijsolstr.2011.10.009.
76. De, M.H. Zeus Tecnología de moleteado ¡ Sin límites ! Available online: https://docplayer.es/62654862-Zeus-tecnologia-de-moleteado-moletas-herramientas-de-moleteado-herramientas-especiales-rodillos-de-brunido.html (accessed on).
77. INTEGI. Knurling & Broaching Technology, Technical Catalogue. 2014. Available online: https://www.toolprocure.com.au/assets/INTEGI_-_Knurling_and_Broaching.pdf (accessed on).
78. INTEGI. Single_Head_Form_Knurling. Available online: https://www.integi.com/en/ (accessed on).
79. Kovalchenko, A.; Ajayi, O.; Erdemir, A.; Fenske, G. Friction and wear behavior of laser textured surface under lubricated initial point contact. *Wear* **2011**, *271*, 1719–1725. https://doi.org/10.1016/j.wear.2011.03.003.
80. Nowell, D.; Hills, D.A. Hertzian contact of ground surfaces. *J. Tribol.* **1989**, *111*, 175–179. https://doi.org/10.1115/1.3261869.
81. Xing, Y.; Deng, J.; Wu, Z.; Wu, F. High friction and low wear properties of laser-textured ceramic surface under dry friction. *Opt. Laser Technol.* **2017**, *93*, 24–32. https://doi.org/10.1016/j.optlastec.2017.01.032.
82. Tewelde, F.B.; Zhou, T.; Zhou, J.; Guo, W.; Zhao, B.; Ge, X.; Wang, W.; Wang, X.; Wang, X. Asymmetric surface texturing for directional friction control under dry sliding condition. *Tribol. Int.* **2023**, *181*, 108321. https://doi.org/10.1016/j.triboint.2023.108321.
83. Chen, J.; Wu, Z. Effect of textured dimples on the tribological behavior of WC/Co cemented carbide in dry sliding with Al_2O_3/WC ceramic. *Micromachines* **2022**, *13*, 1269. https://doi.org/10.3390/mi13081269.
84. Carter, F.W. On the action of a locomotive driving wheel. *Proc. R. Soc. London. Ser. A* **1926**, *112*, 151–157. https://doi.org/10.1098/rspa.1926.0100.

85. Lewis, R.; Dwyer-Joyce, R.S.; Olofsson, U.; Pombo, J.; Ambrósio, J.; Pereira, M.; Ariaudo, C.; Kuka, N. Mapping railway wheel material wear mechanisms and transitions. *Proc. Inst. Mech. Eng. Part F J. Rail Rapid Transit* **2010**, *224*, 125–137. https://doi.org/10.1243/09544097JRRT328.

Disclaimer/Publisher's Note: The statements, opinions and data contained in all publications are solely those of the individual author(s) and contributor(s) and not of MDPI and/or the editor(s). MDPI and/or the editor(s) disclaim responsibility for any injury to people or property resulting from any ideas, methods, instructions or products referred to in the content.